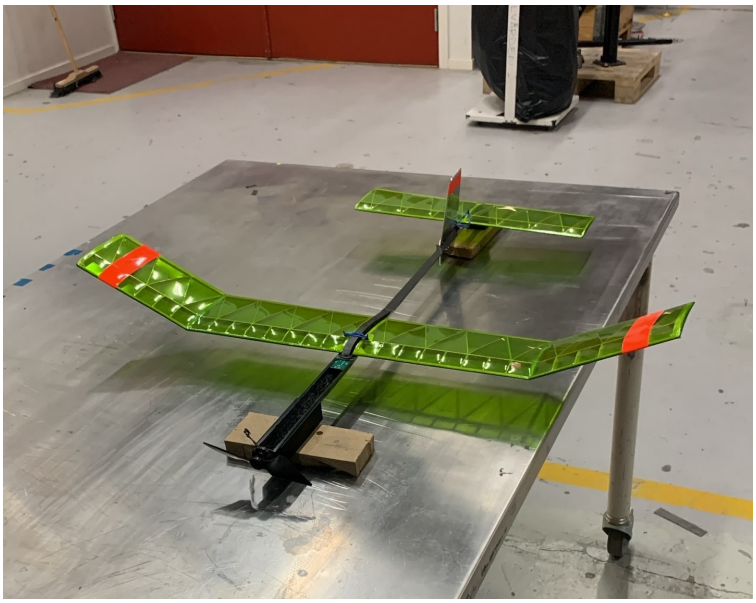

Design and manufacture of a structural battery aircraft demonstrator platform

Design of purpose-made structural battery cells, airframe and propulsion system for a flying structural battery demonstrator

Master Thesis in Industrial and Material Science

Axel Nilsson and Raaed Shajihan

DEPARTMENT OF INDUSTRIAL AND MATERIAL SCIENCE

CHALMERS UNIVERSITY OF TECHNOLOGY
Gothenburg, Sweden 2026
www.chalmers.se

Master Thesis project report 2026

Design and manufacture of a structural battery aircraft demonstrator platform

Design of purpose-made structural battery cells, airframe and propulsion system for a flying structural battery demonstrator

Axel Nilsson and Raaed Shajihan

CHALMERS
UNIVERSITY OF TECHNOLOGY

Department of Industrial and Material Science
Chalmers University of Technology
Gothenburg, Sweden 2026

Design of purpose-made structural battery cells, airframe and propulsion system for a flying structural battery demonstrator platform
Final Report

Supervisor: Leif Asp, Johanna Xu & Richa Chaudhary (Department of Industrial and Material Science), Stefan Lundberg (Department of Electrical Engineering), Tamara Blanco (Airbus S.A.S)
Examiner: Johanna Xu and Leif Asp, Department of Industrial and Material Science

Master Thesis report 2026
Department of Industrial and Material Science
Chalmers University of Technology
SE-412 96 Gothenburg
Sweden
Telephone +46 31 772 1000

Gothenburg, Sweden 2026

Design of purpose-made structural battery cells, airframe and propulsion system for a flying structural battery demonstrator platform
Final Report
Axel Nilsson and Raaed Shajihan
Department of Industrial and Material Science
Chalmers University of Technology

Abstract

Structural batteries are multifunctional materials capable of storing energy while simultaneously carrying significant loads. Although substantial progress has been made in improving both mechanical and electrical performance at cell level, the technology remains underexplored at system level. This report investigates different cell architectures experimentally to create a purpose-designed structural battery cell for an aircraft demonstrator, and prepares a demonstrator platform consisting of custom designed and commercial mechanical and electrical components. This resulted in a flight-ready aircraft platform, ready for flight once the newest structural battery generation has been implemented in the system.

Keywords: structural batteries, aircraft design, composite materials, experimental characterisation, multifunctional materials, Free Flight model aircraft

Acknowledgements

In this project, we have had the chance to explore structural batteries on a system level to a whole new extent. A great challenge, which included many different interdisciplinary challenges. Dealing with these challenges would have been significantly more difficult and less fun, had it not been for all of the very talented people involved.

Firstly, we would like to thank all partners from industry, who have spent a lot of time elaborating on different design ideas and engineering challenges, as well as provided great supervision. A big thank you to Tamara Blanco from Airbus for your supervision and guidance, and a big thank you to Erik Kullgren and Elitkomposit, for providing the Free Flight model, elaborating ideas on manufacturing and aircraft design, and providing us access to your state of the art composite manufacturing plant. This type of industry experience was crucial for us to move this lab-scale work into an engineered aircraft system.

This project has also involved plenty of academic disciplines, with valuable supervision from multiple departments. A big thanks to Stefan Lundberg, for providing great supervision on the electrical engineering side, which allowed an efficient design, manufacturing and validation process on the electrical system. Big thanks to Petter Miltén at the MMS division for providing valuable inputs into the selection and design of the propeller. And last but not the least, a great thanks to Richa Chaudhary, Johanna Xu and Leif Asp for all of the supervision and guidance. We are very thankful for all of the countless of hours you have spent supervising this project, every week.

Lastly, we want to thank Ruben Tavano and Chesta Chesta for all of your advice and brainstorming during both manufacturing and troubleshooting, and Emelie Seignér Bökmark for all of the help with laboratory equipment and our constant order requests for new equipment, components and materials. You have been of great help not only during the thesis, but also our pre-study during the autumn semester.

Axel Nilsson and Raaed Shajihan, Gothenburg June 2026

List of acronyms

Below is the list of acronyms that have been used throughout this thesis listed in alphabetical order:

AC	Alternating Current
BEC	Battery Eliminator Circuit
BLDC	Brushless Direct Current Motor
BMS	Battery Management System
BOM	Bill of Materials
CAD	Computer Aided Design
CC	Constant Current
CE	Coulombic Efficiency
CF	Carbon Fibre
CFRP	Carbon Fibre Reinforced Plastics
CLT	Classical Laminate Theory
CV	Constant Voltage
EECM	Equivalent Electric Circuit Model
EIS	Electrochemical Impedance Spectroscopy
EM	Electric Machine
EPD	Electrophoretic Deposition
ESC	Electronic Speed Controller
EV	Electric Vehicle
FDM	Fused Deposition Modelling
FRP	Fibre Reinforced Plastic
GCD	Galvanostatic Charge Discharge
LCO	Lithium Cobalt Oxide
LED	Light Emitting Diode
LFP	Lithium Iron Phosphate
LIB	Lithium-Ion Battery
LMO	Lithium Manganese Oxide
MFE	Multifunctional Efficiency
MOSFET	Metal Oxide Field Effect Transistor
NE	Negative Electrode
NMC	Nickel-Manganese-Cobalt Oxide
OTS	Off The Shelf
PCB	Printed Circuit Board

PE	Positive Electrode
PWM	Pulse-Width Modulation
RC	Radio Controlled
SEI	Solid Electrolyte Interface
SLS	Selective Laser Sintering
SOC	State of Charge
TP	Test Point
UIUC	University of Illinois at Urbana Champaign
VSD	Variable Speed Drive

Nomenclature

Below is the nomenclature of parameters and variables that have been used throughout this thesis.

Parameters

α	Angle of attack
η	Usability factor
ρ_∞	Density of fluid
τ	Time constant
$\mathbf{A}$	Extensional stiffness matrix
$\mathbf{B}$	Coupling stiffness matrix
$\mathbf{D}$	Bending stiffness matrix
$A_{electrode}$	Area of electrode
c	Aerodynamic chord
$\bar{c}$	Mean aerodynamic chord
C	Capacitance
C_{ah}	Areal capacity of an electrode
C_D	Coefficient of drag
C_{dl}	Double layer capacitance of a battery
C_L	Coefficient of lift
C_M	Coefficient of moment
C_P	Coefficient of power
C_{P0}	Static coefficient of power
C_Q	Coefficient of torque
C_{rate}	C-rate during charge/discharge
C_T	Coefficient of thrust
C_{T0}	Static coefficient of thrust

D	Diameter of propeller
f_p	Frequency at the imaginary impedance peak of a battery
i_{gcd}	Galvanostatic charge-discharge current
J	Advance ratio
n	Rotational speed
n_e	Energy storage efficiency
n_{mfe}	Multi-functional efficiency
n_s	Structural efficiency
q_∞	Dynamic pressure
R	Electrical resistance
R_{ct}	Charge transfer resistance of a battery
R_Ω	Bulk resistance of a battery
S	Reference area
U	Potential
U_{OCV}	Open circuit voltage of a battery
V	Forward velocity
v_∞	Relative airspeed
x_{cg}	Location of centre of gravity
x_{np}	Location of neutral point

Variables

n_p	Number of cells connected in parallel
n_s	Number of cells connected in series
M	Aerodynamic moment
F_{drag}	Drag force
F_{lift}	Lift force
P	Power
Q	Torque
T	Thrust
$\mathbf{N}$	Force matrix
$\mathbf{M}$	Moment matrix
$\varepsilon_\mathbf{0}$	Normal strain matrix
$\kappa_\mathbf{0}$	Curvature strain matrix

Contents

List of Figures

List of Tables

1
Introduction

In a technological landscape in which electrification is driven by the improved maturity of lithium-ion batteries (LIB), system-level optimisations become increasingly relevant. In the automotive industry, for example, electrification leads to large increases in mass at a system level compared to petrol equivalents [1]. As the battery pack can account for up to 25% of a vehicle's total mass [2], multifunctional materials offers a relief in system weight for future vehicle designs.

The problem of "autobesity" is increasingly addressed across different industries. The automotive industry, in particular, has introduced cell-to-body and cell-to-chassis technology to better integrate batteries into the vehicle structure and reduce mass. Although these approaches are sometimes referred to as structural batteries, they do not imply that cells can bear mechanical loads at the cell level, nor that the cells themselves are intrinsically structural. This is where structural battery composite materials, also known as structural batteries, are fundamentally different.

Structural batteries offer the possibility of electrification without a proportional increase in total system weight, by replacing monofunctional elements with multifunctional ones. A structural battery is a multifunctional composite capable of carrying mechanical loads while simultaneously storing energy. To accomplish this type of multifunctionality, carbon fibres are used as a foundation, owing to their good mechanical, electrochemical and electrical properties [3].

During the last few years, significant progress has been made in the field. The second generation of structural battery cells at Chalmers using lithium iron phosphate (LFP) coated carbon fibre in the cathode achieved energy densities on the order of 30 Whkg^{-1} with an elastic modulus of 76 GPa [3]. The most recent generation has seen dramatic improvements from this, with the energy density of structural battery cells now approaching that of conventional LFP cells (unpublished). As this performance gap narrows, demonstration at the system level grows relevant, since the challenges of integrating structural batteries into real engineering systems will eventually need to be addressed.

This thesis aims to represent initial steps toward a structural battery aircraft demonstrator. Specifically, it addresses three interconnected objectives: evaluating purpose-engineered structural battery cells for use in a demonstrator; designing a purpose-built aircraft structure and propeller; and developing the electrical system required for flight.

1.1 Background

Design of an aircraft requires many interconnected design challenges, as the mechanical, electrical and battery system all couple and affect one another. The workflow will therefore include parallel and iterative processes. The workflow is summarized in Figure 1.1.

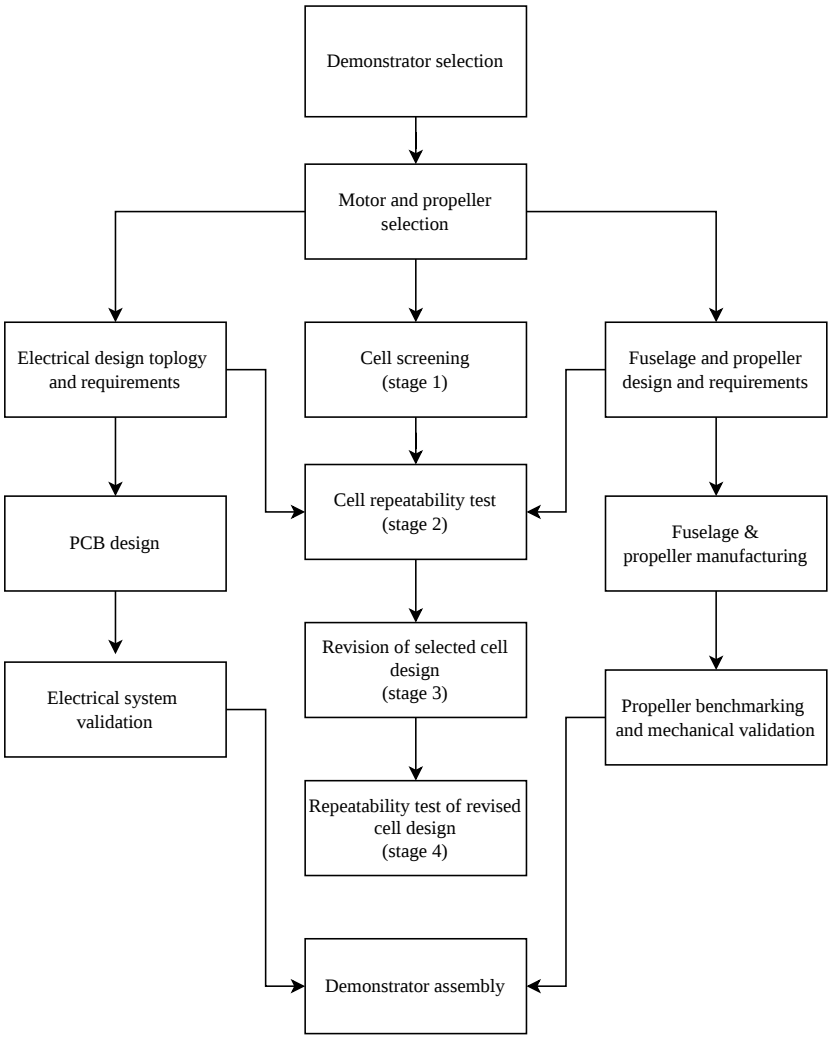

Figure 1.1: Overview of the project workflow.

1.1.1 Selection of demonstrator aircraft

As the number of cells which can be produced, size, and hence also the capacity of these cells are limited, a relatively low power consuming aircraft is desired. Hence, a Free Flight type of aircraft is designed, to allow low power flight and avoid auxiliary power demands from RC communication and flight controls. A balsa based Free Flight aircraft was kindly provided by Erik Kullgren at Elitkomposit, Sweden,

of which the horizontal stabiliser, vertical stabiliser, and wings are kept, and the fuselage is redesigned and replaced. The Free Flight plane uses a 10 g rubber motor, which is to be replaced with an electric motor powered by structural batteries.

1.1.2 Conventional battery cells & composites

LIBs are rechargeable batteries that use dual intercalation electrodes to reversibly move lithium ions between the positive and negative electrode, often referred to as a rocking-chair battery. A LIB consists of a cathode (positive electrode, PE), anode (negative electrode, NE), separator, and an ion conductive electrolyte, generally a lithium salt in a carbonate solvent [4]. The graphite anode remains the dominant choice in state-of-the-art lithium-ion batteries, while cathode chemistries are commonly grouped into three main classes: layered oxides (e.g., LCO, NMC), which are valued for their high energy density; spinel cathodes (e.g., LMO), which offer high-rate capability because of their three-dimensional Li-ion diffusion pathways; and olivine cathodes (e.g., LFP), which are prized for their high structural stability, safety, and long cycle life [5], [6], [7].

A composite material is a material system where two or more constituent materials are combined together macroscopically to form a new material with desirable properties [8]. Fibre Reinforced Plastic (FRP) is an example of a widely used composite material. FRPs normally consist of a fibre reinforcement, which acts as the main mechanical load bearing member due to its high stiffness and strength. The matrix material bonds together these fibre reinforcements and transfer mechanical load between fibres while protecting them from the environment outside. The fibres or matrix alone are not of much use, but they can be combined together to form much more desirable properties like enhanced strength and stiffness at lower densities compared to metals. Carbon Fibre Reinforced Plastics (CFRP) are an example of composite materials and they are used widely in the aerospace industry for their superior strength and stiffness by weight ratios [8].

1.1.3 Structural battery composites

A structural battery is a type of multifunctional composite which combines the functions of the conventional LIB with that of conventional carbon fibre composites [3]. In this design, carbon fibres (CF) are used as active negative electrodes, and LFP coated CF are used as positive electrodes, whereas a lithium-ion (Li-ion) conductive semi-solid polymer electrolyte matrix, referred to as a Structural Battery Electrolyte (SBE) acts as mechanical load transfer between fibres and for ion transport and electrical insulation between electrodes.

When replacing a structure and a battery with a multifunctional composite, the mass savings are determined by the multifunctional efficiency (MFE) of the material. The MFE is described as

$$n_{mfe} = n_s + n_e \tag{1.1}$$

where n_{mfe} is the MFE, n_s is the structural efficiency of the material compared to the conventional structure, and n_e is the energy storage efficiency compared to the conventional energy storage the multifunctional material replaces [9]. In order to achieve a mass saving, the MFE must be greater than one. Hence if the multifunctional material is just as good of a battery and a structure as the material it replaces, the MFE is 2, and the mass of the system is halved.

At Chalmers University of Technology, two generations of structural batteries have been developed to date. The first one, uses a commercial LFP foil as positive electrode and a Whatman separator. Due to only the negative electrode providing load bearing capabilities, and the use of a thick Whatman separator, this cell reached an elastic modulus of 25 GPa and an energy density of 24 Whkg^{-1}, which equates to a low MFE [2].

The second generation, introduced at the end of 2024, was the first all-fibre battery. By using Electrophoretic deposition (EPD), the fibres could be coated with LFP particles to create a counter electrode to the T800 fibre on the negative electrode. Additionally, by replacing the Whatman separator with a thin cellulose separator, the performance saw great improvements with an energy density of 30 Whkg^{-1} and an elastic modulus of 76 GPa. This dramatically increased the MFE of the material to approximately 0.88 [3]. The differences between these two generations are visualised in Figure 1.2.

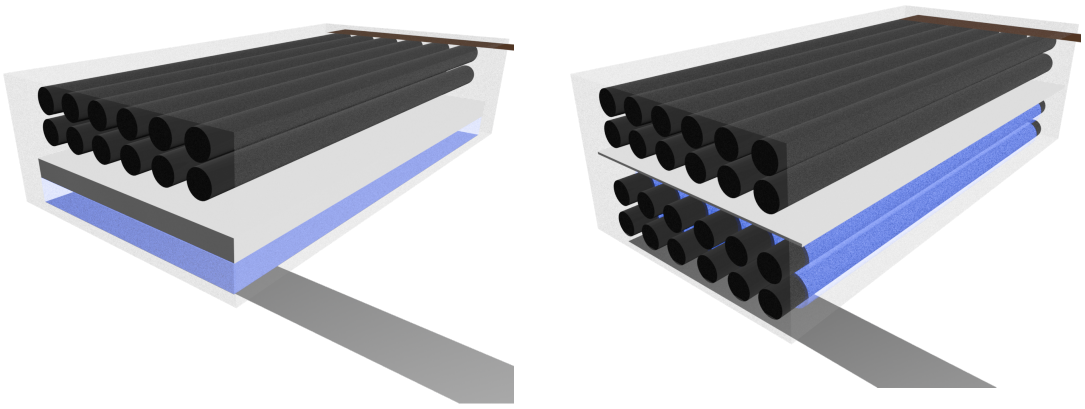

(a) **(b)**

Figure 1.2: (a) First generation structural battery from Chalmers University of Technology, utilising a commercial positive electrode, (b) second generation structural battery from Chalmers University of Technology, utilising EPD to coat CF with LFP, hence creating the first all-fibre battery.

Although the second generation provides significantly better multifunctional performance, the additional EPD coating procedure to manufacture the positive electrodes made it unsuitable for this project. Hence, the first generation is chosen,

with a slight modification that a cellulose separator is used instead of a Whatman separator, hence ideally increasing the energy density from what has been reported for that generation.

1.1.4 Structural battery systems and demonstrators

The structural battery cells developed at Chalmers University of Technology have previously been demonstrated as multicell laminates in two different studies, one in which Siraj and Tasneem et al. developed the current manufacturing method for structural battery composites [10], and one study from Xu et al. in which a multi-cell laminate was prepared for thorough mechanical and electrical testing [11]. The most recent work demonstrated the structural cell in a mechanical and electrical system, by integrating three structural battery cells in a torch frame, from which they could power the LED of the torch (unpublished).

Another type of multifunctional composites referred to as structural supercapacitors, has been thoroughly demonstrated. A recent demonstrator from Imperial College London, showed how structural supercapacitors integrated into the C-beam of an Airbus A380 Aircraft, can replace the monofunctional supercapacitors to power the aircraft door, which opens the door in case of an emergency and power outage. The demonstrator uses multiple structural supercapacitors which are externally connected in series to provide sufficient voltage to the servo motor to open the aircraft door. This demonstrator shows how multifunctional composites are capable of powering servo motors, an important milestone and relevant finding in order to demonstrate the technology in a moving demonstrator [12].

1.2 Aim and research questions

The aim of the thesis is to explore cell and pack level architectures for structural batteries suitable for integration into an aircraft demonstrator, and to build a platform for such a demonstrator that is ready for structural battery integration. This task includes the following research questions:

- What aircraft structures are suitable for the integration of structural batteries?
- Which structural battery cell design (size, stacking concept, positive electrode choice) provides the best trade-off between energy density, power capability and integrability for the chosen demonstrator?
- Is it possible to integrate structural batteries into load bearing structures of the demonstrator to save weight?
- How should the electrical system and control strategy be designed to ensure safe operation (current limits, balancing, protection) while meeting the demonstrator's performance requirements, and to what extent can this be implemented with commercially available components?

1.3 Scope and limitations

The scope of the thesis is limited to the time frame, as cell manufacturing processes such as drying and conditioning fundamentally takes time. One time saving measure included is the choice of only using available commercial positive electrodes, as manufacturing of structural carbon fibre positive electrodes is time consuming, and requires training.

2
Theory

2.1 Cell materials and manufacturing

Manufacturing of structural battery composites combines methodologies used when manufacturing batteries and carbon fibre composites, and a process was developed during 2022 for better consistency [10]. Here, the methodology, using vacuum infusion and cell pouching is adopted. When designing cells which are to be used in a system, further manufacturing methods are implemented from commercial cell manufacturing, the main one being cell stacking.

Cell stacking is commonly used for pouch cell manufacturing, when the alternative, jelly roll manufacturing, which is most commonly used for prismatic and cylindrical cells, is not desired [13]. Stacking and jelly rolling is crucial to maximise the capacity of one cell and hence minimise the parasitic weight. Similarly, stacking of composites can provide improved mechanical characteristics increasing the incentive to pursue stacking in structural battery composites. Stacking can be performed both before and after the infusion of individual cells. If the stacking is done before infusion, the structural battery sees an improvement in both mechanical and electrical performance. But if the stacking is done after infusion, the structural battery will only see an improvement in the electrical aspect and not the mechanical aspect due to the lack of any inter-laminar shear strength. This can be corrected by cobonding them at a later stage [8].

2.2 Electrochemical characterisation

During the first few cycles of a newly manufactured cell, the solid electrolyte interface (SEI) forms at the negative electrode. During this process, lithium inventory is lost. Although leading to an initial capacity loss, the process is crucial to create a stable battery with high coulombic efficiency (CE) [14].

In order to form this layer, numerous galvanostatic charge and discharge (GCD) cycles are generally performed at low charge rates (C-rates), typically around C/20 for structural batteries. The charge rate at the first two evaluation stages is calculated from the usable capacity of similar cells previously reported in the literature, such as [10]. In this paper, the usable capacity proved to be ≈ 30 % of the specified areal capacity of the LFP foil. The charging current for the GCD

cycling is calculated as

$$i_{gcd} = C_{Ah} \cdot \eta \cdot A_{electrode} \cdot C_{rate} \tag{2.1}$$

where i_{gcd} is the charging current, C_{Ah} is the areal capacity specified from the LFP foil, η is the usability factor, $A_{electrode}$ is the active area of the cell and C_{rate} is the desired C-rate for the GCD. For the third and fourth evaluation stages, η=1 was assumed, as a cycling approach with a low η led to very extended first charging cycles.

If full cell capacity is to be utilised, it is advantageous to include a constant-voltage phase in the charge cycle. As the voltage required to maintain the set charging current approaches the programmed cut-off voltage, the charging process can switch from constant current to constant voltage, where the voltage is held at the cut-off level to continue charging the cell at a decreasing current. This allows the cell to reach the remaining 20–30% of its state of charge (SOC). A similar stage can be added to the discharge cycle if complete discharge is desired [15].

In order to create Equivalent Electrical Circuit Models (EECM) from battery cells, batteries are often characterised using Electrochemical Impedance Spectroscopy (EIS). EIS is performed using a galvanostat, and can be performed galvanostatically or potentiostatically. By exciting the battery using an alternating current (AC) or voltage and measuring the response, a circuit model can be fitted. The data is generally presented in a Nyquist plot [16]. The complexity of different EECMs may vary significantly. Popular models include the Rint Model, the simplified Randles Model, and the second order Thevenin Model. These are all visualised in Figure 2.1.

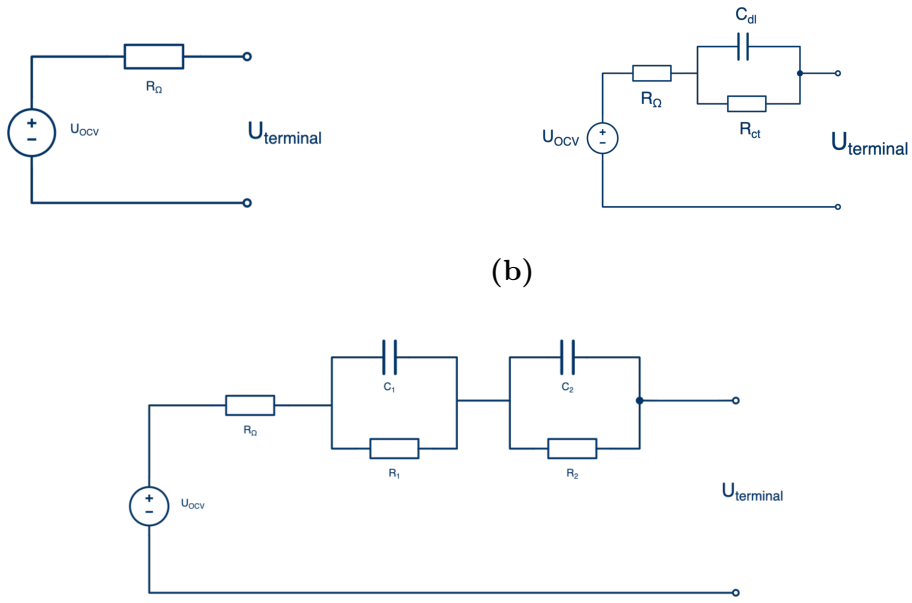

(a) **(b)**

(c)

Figure 2.1: (a) EECM of the Rint model, (b) EECM of the simplified Randles model, (c) EECM of the second order Thevenin model.

The Rint model can be used by only considering the bulk resistance. This model is useful when simulating the steady state IR drop of the cell, and for making simple SOC estimations if the current is known.

The simplified Randles model uses the additional charge transfer resistance, R_{ct}, and the double-layer capacitance, C_{dl}, and captures the transient behaviour of the cell. From the perspective of the Nyquist plot, that equates to the first semi-circle. If the electrochemical properties are to be modelled in more detail, an additional Warburg Impedance can be added after the RC-element to model the diffusion. However, this depth of modelling is not necessary for SOC estimation [17].

When a second semi-circle is distinguishable in the Nyquist plot, a second order Thevenin Model can be used. However, for the case of structural batteries, this semi-circle is rarely visible.

In this report, the Rint model and the simplified Randles model are used exclusively. Identifying the R_Ω, is done simply by studying the real impedance when the imaginary impedance is zero in the Nyquist plot. The R_{ct} is found by graphically determining the diameter of the semi-circle. From the highest point of this circle, it is known that

$$2\pi f_p \tau = 1 \tag{2.2}$$

where f_p is the frequency at the peak of the semi-circle and τ is the time constant. Since the time constant can simply be expressed as

$$\tau = RC \tag{2.3}$$

the double layer capacitance in the first order Thevenin Model can be calculated as

$$C_{dl} = \frac{1}{2\pi f_P R_{ct}} \tag{2.4}$$

which completes the equivalent circuit. [18]

2.3 Electrical systems in battery-powered applications

The complexity of the electrical system may vary significantly depending on the application. Propulsion systems designed to operate within a broad spectrum of rpms, often referred to as Variable Speed Drives (VSD), have multiple constituents in common.

The pre-charge circuit is a common part of VSDs, especially in EV applications. Pre-charge circuits are needed especially in high voltage due to the high capacitive loads causing very high inrush currents, which may damage components or cause unnecessary stress to the battery cells. The most common pre-charge circuits uses a pre-charge contactor which drives the current through a power resistor and limits the current. In steady state, the contactor is disconnected and a regular contactor connects the batteries to the system. If the voltage level is lower, the contactors can be replaced by semiconductors, such as a Metal Oxide Field Effect Transistor (MOSFET). The implementations may vary, and multiple transistors can be connected in parallel if necessary [19].

Two key constituents in drive systems are the Electronic Speed Controller (ESC) and the Electric Machine (EM). In state-of-the-art EVs, the most common choices for electric machines are permanent magnet synchronous machines, due to their low weight, compact size, and high efficiency. Popular alternatives include induction machines and electrically excited synchronous machines, the latter of which has recently gained market share. However, within the smaller radio-controlled space, brushless direct current motors (BLDC) have been dominant for a significant time [20].

The functionality of the ESC depends on the type of EM employed. BLDC and AC motors require three-phase excitation of their stator windings. In BLDC motor drives, the ESC operates as a three-phase inverter that applies a sequence of voltage waveforms to the motor windings. Commutation is achieved by selectively switching semiconductor devices within the inverter, thereby generating a rotating magnetic field that interacts with the permanent magnets of the rotor. The commutation sequence is illustrated in Figure 2.2. Motor speed is typically regulated through Pulse Width Modulation (PWM), which adjusts the effective voltage applied to the windings.

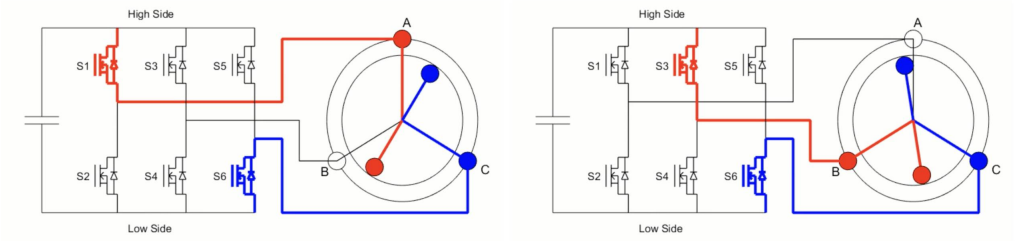

Figure 2.2: Illustration of BLDC motor commutation.

Source: [21]

The ESC receives a control signal from an external controller, which in radio-controlled (RC) applications is commonly generated by a radio receiver. Traditionally, this command signal consists of a periodic pulse train with a repetition frequency of approximately 50 Hz, where the pulse width represents the requested motor speed or throttle setting.

Due to the widespread use of BLDC motors in RC applications, commercially available OTS ESCs are readily available and therefore represent a practical solution for the moving structural battery demonstrator investigated in this work. In addition to performing motor control and power conversion, many ESCs incorporate auxiliary power-supply functionality for onboard electronics. Since subsystems such as radio receivers typically require a regulated supply voltage that differs from the motor supply voltage, ESCs often integrate a Battery Eliminator Circuit (BEC), which provides a regulated output voltage, commonly 5 V [22]. This auxiliary supply is frequently used to power radio receivers, servos, and other low-power electronic devices. In fixed-wing RC aircraft, servos powered by the BEC are commonly used for actuation of control surfaces. The main functions and electrical interfaces of the ESC are illustrated in Figure 2.3.

Figure 2.3: Pinout of the ESC, with motor phases A-C, BEC, battery connectors and PWM speed signal.

When selecting a BLDC motor, one important parameter is the KV rating, which specifies the motor's no-load rotational speed per applied volt (rpm/V). Higher KV ratings correspond to higher achievable rotational speeds but generally lower torque

per ampere. In small drone applications, particularly micro quadcopters, motors with KV ratings of up to 27,000W rpm/V are commercially available [23].

2.3.1 Battery management systems

The battery management system (BMS) of a battery pack is a key component, especially with Lithium-ion technology, as overcharging and undercharging can cause a battery fire. As each cell has underlying inconsistencies from manufacturing and undergo different temperature cycles during operation in the battery pack, it is necessary to individually monitor each cell. A BMS continuously monitors current, voltage and temperature, and can detect imbalanced cells from measuring the voltage from each series connected string. To balance uneven charge distribution, a BMS can use active or passive balancing. Active balancing redistributes charges from higher charged strings onto the strings with a lower charge level, whereas passive balancing dissipates the energy of the fully charged cells and allows the lower charged cells to reach the same voltage. Passive balancing is only necessary during the charging process, which means that it can be handled by an external charging circuit [24].

2.3.2 Modelling the battery pack from Randles model

From the Randles model presented in Section 2.2, an equivalent circuit model of the battery pack can be constructed to estimate its electrical performance. The pack model is obtained by combining individual cell models according to the physical series and parallel configuration of the battery pack.

If all cells are assumed to exhibit identical electrochemical behaviour, the pack model can be derived by directly scaling the parameters of a single Randles cell. Alternatively, individual cell models may be replicated and interconnected to represent the complete pack when investigating the influence of cell-to-cell variations in parameters or state of charge.

In this work, the primary quantity of interest is the terminal voltage response during discharge. The propulsion system requires a specified average current, and excessive voltage drop may reduce the available power or trigger the BMS undervoltage protection. Therefore, equivalent circuit parameters are derived for both parallel-connected cell groups and the complete battery pack.

For a cell group consisting of n_p identical cells connected in parallel, the equivalent Randles parameters become

$$R_{\Omega,n_p} = \frac{R_\Omega}{n_p} \tag{2.5}$$

$$R_{ct,n_p} = \frac{R_{ct}}{n_p} \tag{2.6}$$

$$C_{dl,n_p} = n_p \cdot C_{dl} \tag{2.7}$$

These relationships follow directly from the electrical behaviour of parallel-connected circuit elements, where resistances decrease and capacitances increase with the number of parallel branches. Physically, the parallel-connected cells share the applied current, reducing the effective internal resistance while increasing the available charge-storage capability represented by the double-layer capacitance.

The battery pack is subsequently formed by connecting n_s identical cell groups in series. The equivalent pack parameters can therefore be expressed as

$$R_{\Omega,eq} = n_s \cdot R_{\Omega,n_p} \tag{2.8}$$

$$R_{ct,eq} = n_s \cdot R_{ct,n_p} \tag{2.9}$$

$$C_{dl,eq} = \frac{C_{dl,n_p}}{n_s} \tag{2.10}$$

Series connection increases the voltage capability of the battery pack while also increasing the equivalent resistance. The equivalent double-layer capacitance decreases according to the same relationship as conventional capacitors connected in series.

The resulting equivalent circuit, representing a battery pack consisting of n_s series-connected cell groups with n_p parallel-connected cells per group, is illustrated in Figure 2.4.

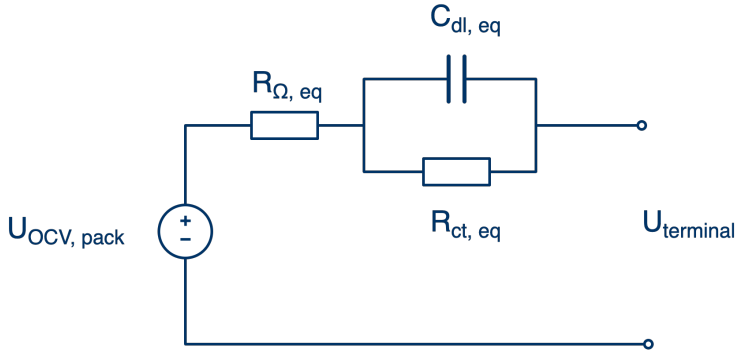

Figure 2.4: Equivalent circuit representation of a battery pack consisting of n_p parallel-connected cells per group and n_s series-connected cell groups.

2.4 Mechanical systems in aircraft applications

Building a Free Flight model aircraft powered by structural batteries introduces mechanical challenges with respect to the structure of the fuselage, propeller

selection and stability of the aircraft since the fundamental mode of energy storage and propulsion is now different.

2.4.1 Aerodynamic forces and moments on an aircraft

Aerodynamic lift and drag are two primary forces an aircraft experiences as it moves through air. Aerodynamic lift produces a net force F_{lift} perpendicular to the direction of relative airflow and is caused due to the pressure difference between the upper and lower surface of an aerofoil. A drag force F_{drag} acts parallel to the direction of relative airflow, and opposes the aircraft's movement through air. Drag arises from a pressure difference between the front and rear of an aerofoil, and due to skin friction. An aerofoil also experiences a moment M due to the surface pressure and shear stress distribution that tends to rotate the wing. This moment M can be calculated about any point in the aerofoil. These forces and moments are visualised in Figure 2.5 and can be quantified as

$$F_{lift} = C_L q_\infty S \tag{2.11}$$

$$F_{drag} = C_D q_\infty S \tag{2.12}$$

$$M = C_M q_\infty S c \tag{2.13}$$

where S is the reference area, and c is the chord length, C_L, C_D, and C_M are the coefficients of lift, drag, and moment respectively. They are dependent on the angle of attack α, Reynolds Number, and geometry of the aerofoil. The ratio between C_L and C_D is defined as the L/D ratio. q_∞ is the dynamic pressure and is quantified as

$$q_\infty = \frac{1}{2}\rho_\infty v_\infty^2 \tag{2.14}$$

where ρ_∞ is the density of the fluid and v_∞ is the relative velocity between the fluid and the aerofoil [25].

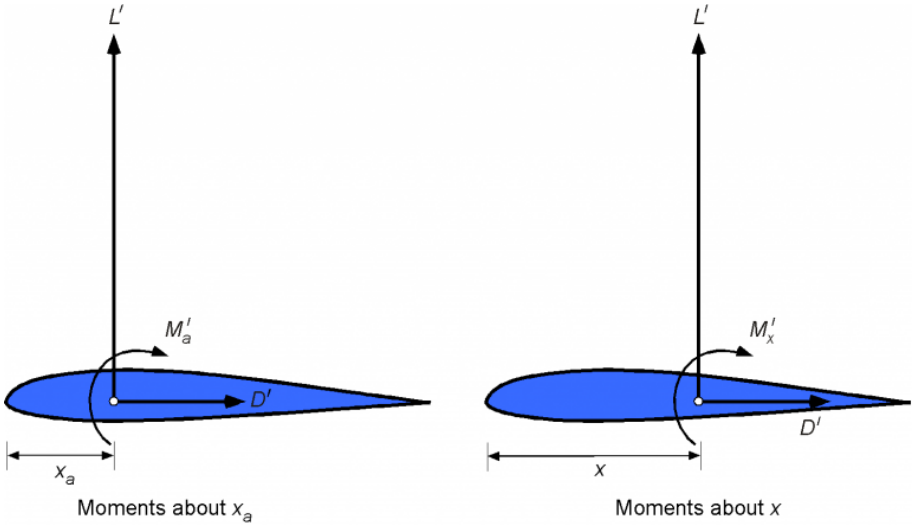

Figure 2.5: Forces and moments on an aerofoil about 2 points x_a and x.

Source: [26]

2.4.2 Aircraft stability

Aircraft stability is divided into two types: static and dynamic stability. These concepts are described in detail by Anderson [25].

Static stability is determined by the reaction of a body to disturbances to its equilibrium state and can be divided into three sub-types: positive static stability, negative static stability, and neutral static stability. If the forces and moments acting on a body after a disturbance is applied on it works to bring the body back to its original equilibrium position, the body is said to have positive static stability. If the forces and moments on a body after a disturbance is applied to it works to move the body away from its original equilibrium position, the body is said to have negative static stability. If there are no forces and moments on a body after a disturbance is applied to it and it remains in this new state of equilibrium, the body is said to have neutral static stability. Figure 2.6 visualises this concept on an aircraft.

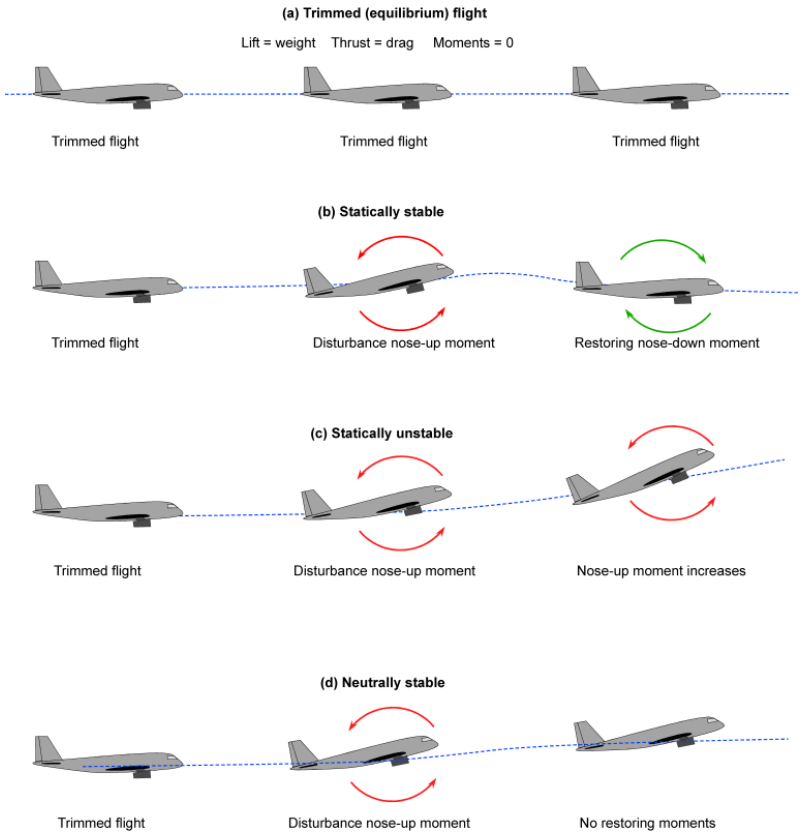

Figure 2.6: Illustration of positive, negative, and neutral static stability.

Source: [26]

Dynamic stability depends on the time history of a body's response to a disturbance after it has initially responded to its static stability. It refers to the ability of a body to return and remain at its equilibrium position over a long period of time. It should be noted that positive static stability is a necessary but not sufficient condition for

dynamic stability. Similar to static stability, dynamic stability is also classified into positive, negative, or neutral dynamic stability. Figure 2.7 visualises this concept for an aircraft.

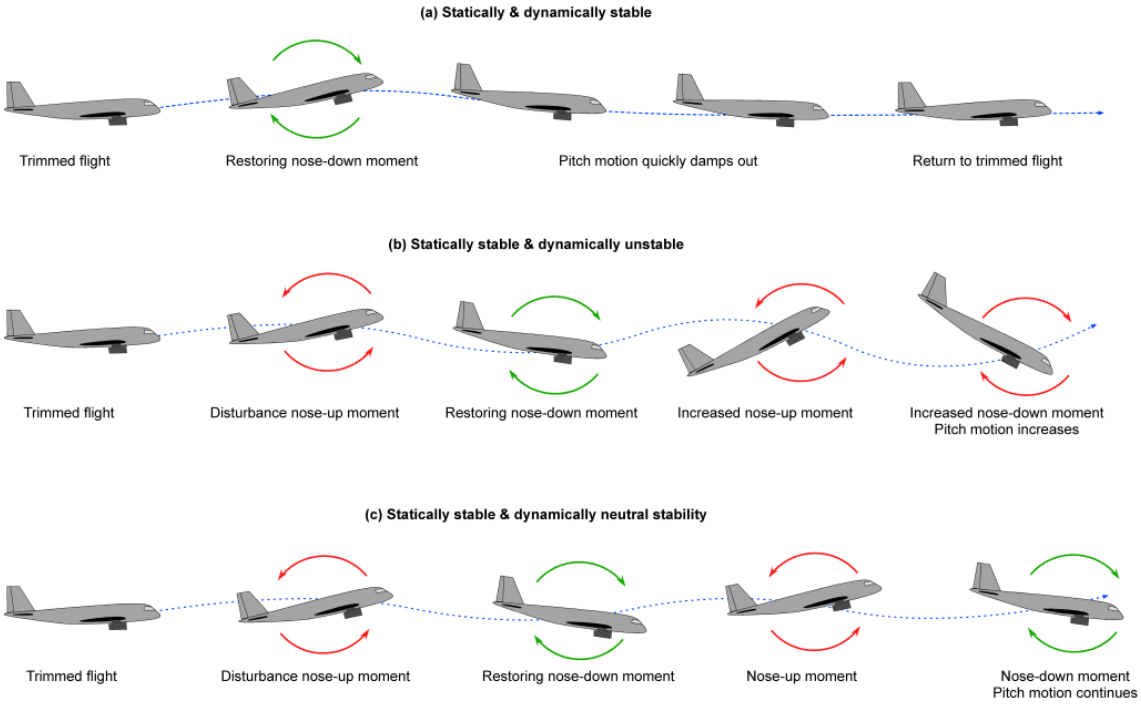

Figure 2.7: Illustration of positive, negative, and neutral dynamic stability.

Source: [26]

For a Free Flight aircraft, longitudinal static stability is of much greater concern than lateral or directional stability since the aircraft is symmetric about the centre and there is no active control on the aircraft. For a conventional wing-tail configuration, static longitudinal stability requires that the pitching moment co-efficient C_M decreases with increasing angle of attack α, i.e, $\frac{\partial C_M}{\partial \alpha} < 0$ [25]. The pitching moment about the centre of gravity can be expressed as

$$\frac{\partial C_{M,cg}}{\partial \alpha} = \frac{\partial C_L}{\partial \alpha} \frac{x_{cg} - x_{np}}{\bar{c}} \tag{2.15}$$

where $\frac{\partial C_L}{\partial \alpha}$ is the change in coefficient of lift C_L with angle of attack α, x_{cg} is the position of the centre of gravity, and x_{np} is the position of the neutral point and $\bar{c}$ is the mean aerodynamic chord. Since $\frac{\partial C_L}{\partial \alpha}$ is positive (in the operating angles of attack of the aircraft), $x_{cg} - x_{np}$ has to be negative, i.e, the location of the centre of gravity has to be in-front of the location of the neutral point of the aircraft.

2.4.3 Propellers and power requirements

Propellers convert rotational power provided by a power source like an electric motor into thrust by accelerating the air passing through it backwards. It has a

number of blades that acts as rotating wings, effectively producing lift in the axis of rotation of the blades, which is perceived as thrust.

Even though many theories exist to calculate the thrust produced by a propeller, it is commonly defined according to the Momentum-Blade Element Theory [27] as

$$T = C_T \rho n^2 D^4 \tag{2.16}$$

where ρ is the density of the fluid, n is the rotational speed (in revolutions per second), D is the diameter of the propeller, and C_T is the coefficient of thrust, which is a non-dimensional quantity. The coefficient of thrust C_T is a function of the advance ratio J such that $C_T = C_T(J)$.

$$J = \frac{V}{nD} \tag{2.17}$$

where V is the forward velocity of the aircraft/propeller.

Power, P, and Torque, Q, are calculated as:

$$P = C_P \rho n^3 D^5 \tag{2.18}$$

$$Q = C_Q \rho n^2 D^5 \tag{2.19}$$

where C_P and C_Q are coefficients of power and torque respectively. Hence, thrust, power, and torque for a given operating point are all calculated from empirical propeller test data.

2.4.4 Composite structures in aircrafts

Composites like carbon fibre reinforced plastics (CFRP) are widely used in the aerospace industry due to their superior specific strength and stiffness compared to traditional materials like Aluminium and Steel. But the highly directional properties of these materials bring forth challenges in the design and analysis of composite components.

Classical Laminate Theory (CLT) aims to simplify this process by describing the mechanical behaviour of a laminated composite by combining the contributions of the individual plies or laminae [8]. It assumes linear elastic behaviour and perfect bonding between layers and is formulated as:

$$\begin{Bmatrix} \mathbf{N} \\ \mathbf{M} \end{Bmatrix} = \begin{bmatrix} \mathbf{A} & \mathbf{B} \\ \mathbf{B} & \mathbf{D} \end{bmatrix} \begin{Bmatrix} \boldsymbol{\varepsilon}_0 \\ \boldsymbol{\kappa} \end{Bmatrix} \tag{2.20}$$

where $\mathbf{A}$ is the extensional stiffness matrix, $\mathbf{B}$ is the coupling matrix, and $\mathbf{D}$ is the bending stiffness matrix. For laminates exhibiting symmetry about its mid-plane, the coupling matrix is zero and hence effective in-plane properties like Young's modulus, shear modulus, and Poisson's ratio can be calculated from the $\mathbf{A}$ matrix.

3
Methodology

3.1 Cell development and evaluation

The cell development is performed in four stages: two screening stages separated by repeatability testing of the selected configuration, with electrochemical impedance spectroscopy and cycling as the principal characterization methods.

- **Stage 1:** Screening of initial cell layouts
- **Stage 2:** Repeatability tests of the best performing layout
- **Stage 3:** Screening of improved cell design
- **Stage 4:** Repeatability tests of the selected improved design

3.1.1 Stage 1: Screening of cell layouts

Stage 1 is used to screen geometry, stack concepts and cathode chemistries. This stage provides design freedom to test concepts used in commercial battery cell and composite manufacturing in order to engineer purpose-built cells for a demanding application.

The chosen aircraft design requires a cell format that can provide enough capacity while still fitting in the fuselage. For that reason, one of the key concept evaluated in stage 1 is stacking. It is a familiar principle used in both pouch-cell manufacturing and composite layups, and is therefore very relevant. It is also a natural continuation of the work done with the structural battery torch, where stacking was demonstrated with individually cured structural battery laminates.

Here, a stacked layup of two layered cells, utilising a double layer carbon fibre in the middle of the stack, and LFP foils at the bottom and top of the stack is evaluated first. Hence the carbon fibre electrodes can be lithiated from both sides, and only one current collector is needed for the negative electrode. This PE-NE-NE-PE layup, is visualised in Figure 3.1a. In the figure, the double layered carbon fibre can be seen, with the current collector between the two layers, along with the two opposite facing positive electrode and the z-stacked separator.

The manufacturing of the positive electrode is identical to that reported by Siraj et al. [10], and the double layered carbon fibre negative electrode is manufactured by silver gluing one carbon fibre tape to both of the sides of a copper current collector. The negative electrode is subsequently wrapped in the z-stacked separator. The layup in the vacuum bag was simplified using jigs.

This manufacturing process is summarized in Figure 3.1. The limitations of the Z-stacked double layered cell is also evaluated by manufacture of a four layered cell, to investigate if an increasing number of layers will affect the carbon fibre wetting, the LFP foil encapsulation effect, and hence the charge transfer resistance R_{ct}. The stacking is visualised in Figure 3.2.

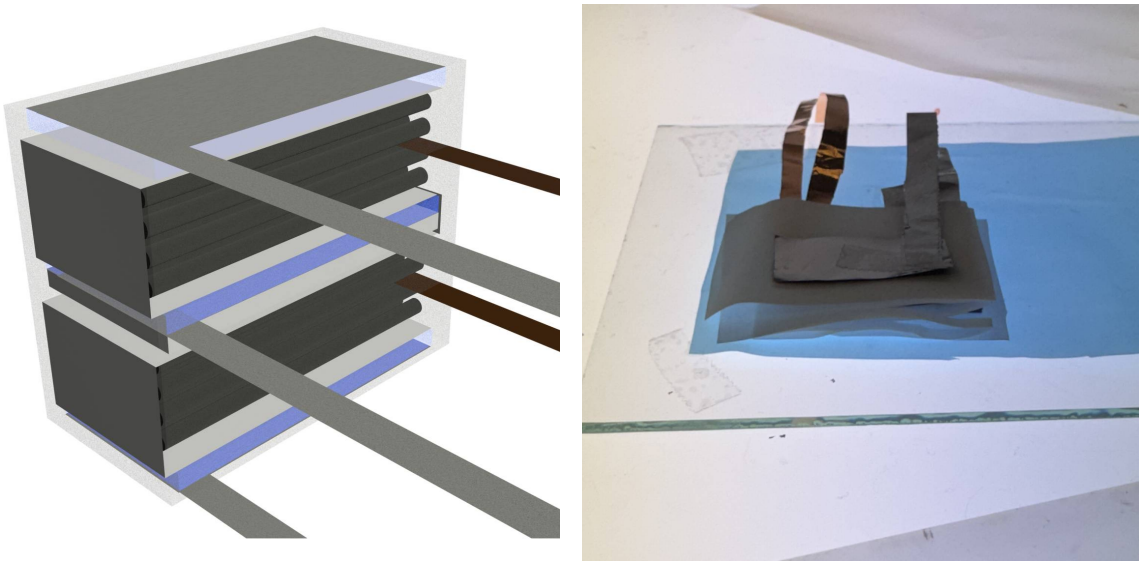

(a) **(b)**

Figure 3.2: (a) Illustration of a four layered structural battery cell with 2 double-layered negative electrodes, 4 positive electrodes and a z-stacked separator folded along the short side, (b) assembly of a four layered structural battery cell.

The addition of a dwell time is further considered, to allow an even distribution and complete wetting of the carbon fibre, by waiting 5 hours from infusion to curing.

In addition, the use of layered oxides cathodes, specifically power optimised NMC111, with an areal capacity of 1 mAhcm^{-2}, similar to the commercial LFP foil is explored. NMC offers greater conductivity, due to its 2D diffusion channels, as well as higher voltage and hence an improved energy density.

In the first stage, EIS is only conducted after the successful conditioning of ten GCD cycles.

3.1.2 Stage 2: Repeatability tests of the selected layout

In stage 2, the best performing layout is chosen and produced in many examples, to test repeatability and the possibility of aircraft implementation. In this stage, slight modifications are made in terms of dimensions in order to fit into the aircraft. Additionally, the copper current collector is moved towards the middle of the electrode, to minimise the distance each electron has to move in the carbon fibre and hence reduce the resistive losses in the negative electrode. The electrodes are vacuum bagged two and two, allowing four cells to be infused at the same time with

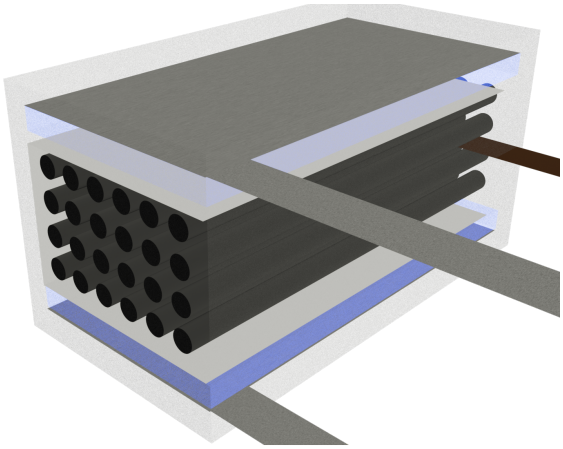

(a)

(b)

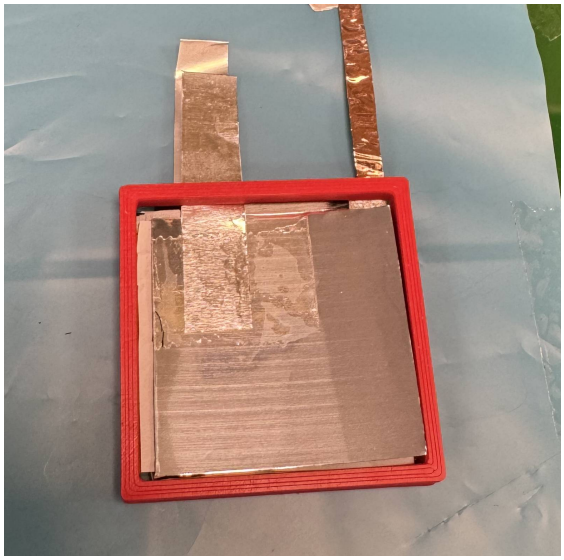

(c)

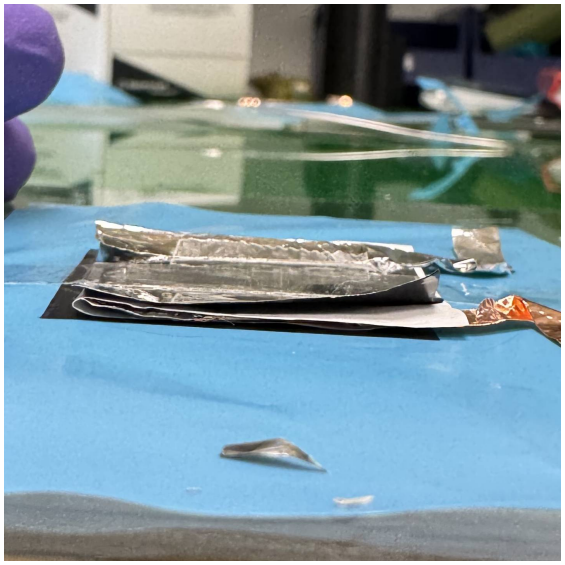

(d)

Figure 3.1: (a) Schematic of the two layered stacked cell with a z-stacked separator and a double layered negative electrode, (b) manufacturing procedure for double layered negative electrode, (c) top view of double layered cell during manufacturing using a 3D-printed fixture for easier alignment, (d) side view of double layered cell during manufacturing.

2 vacuum pumps. The vacuum bags, along with the modified negative electrode are shown in Figure 3.3.

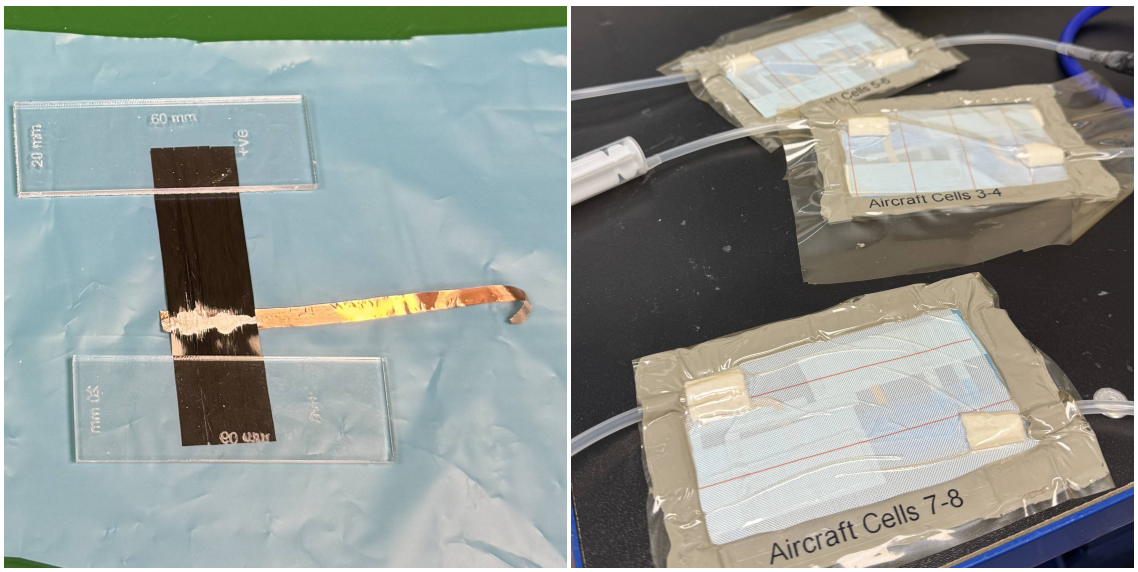

(a) **(b)**

Figure 3.3: (a) Manufacturing of negative electrode with centralised current collector for stage 2 cell, (b) vacuum bag infusion of stage 2 cells.

After curing, 400 µL of liquid electrolyte is added to the pouch along with the cured cell, and before conditioning, each cell undergoes potentiostatic EIS, to make sure that the manufacturing is executed correctly.

3.1.3 Stage 3: Revision of selected cell layout

In stage 3, the design is revised, and specifically methods to improve carbon fibre wetting are evaluated. These include extending the carbon fibre outside of the LFP-foil, and adding pinholes to the foil to prevent an encapsulating behaviour from the two foil layers under vacuum. Additionally, an additional drying stage is added, in which all electrodes are dried overnight at 90 °C, to further suppress moisture prior to vacuum bagging. The positive electrode with pinholes, along with a cured cell visualising the carbon fibre extending outside of the positive electrode, are visualised in Figure 3.4.

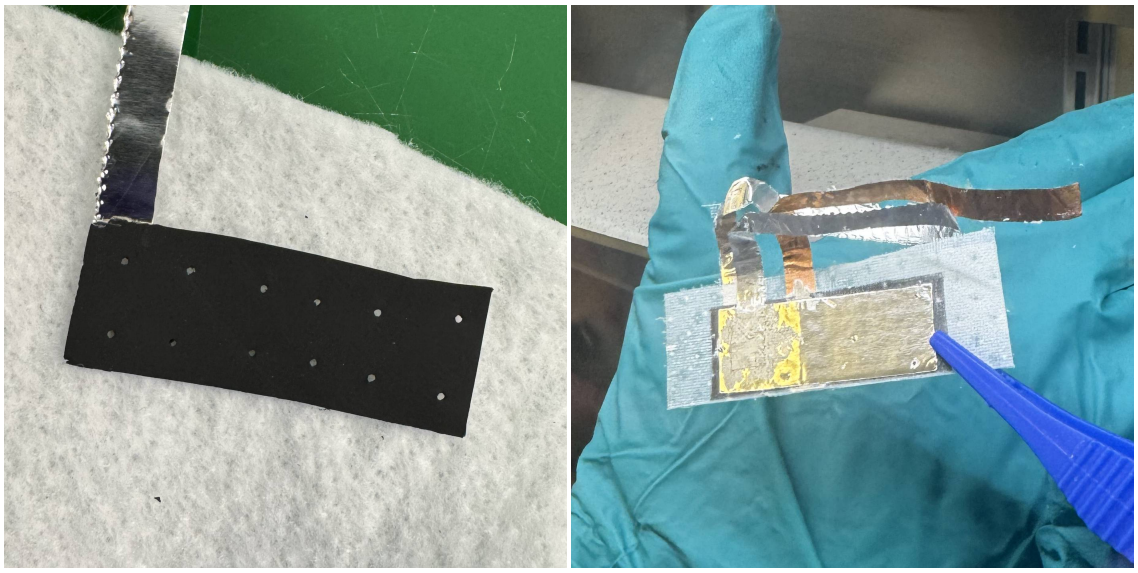

(a) **(b)**

Figure 3.4: (a) Positive electrode with pinholes, used in stage 3, (b) cured cell with extended negative electrode and a positive electrode with pinholes.

The pinhole configuration is evaluated on both stacked and simple single layer cells, and compared. 400 µL of electrolyte is added to the stacked cells, whereas only 200 µL is used for the single layer cells. EIS is conducted on all cells prior to conditioning.

3.1.4 Stage 4: Repeatability test of revised design

Finally, in stage 4, a revised design is evaluated with a repeatability test, with the possibility of aircraft implementation.

This stage includes the additional drying stage from stage 3 and keeps the pinhole concept of the positive electrode foil. Double layer cells are abandoned in favour of simple, single layer cells. Manufacturing uses larger vacuum bags in order to manufacture several cells at the same time. In this stage, four vacuum bags of cells are completed, three of which use the larger vacuum bag capable of fitting six cells, pictured in Figure 3.5. The first large vacuum bag, uses a two inlet and two outlet configuration, whereas the last two use a two inlet one outlet configuration. This means a total of 20 manufactured cells, of which 18 are tested.

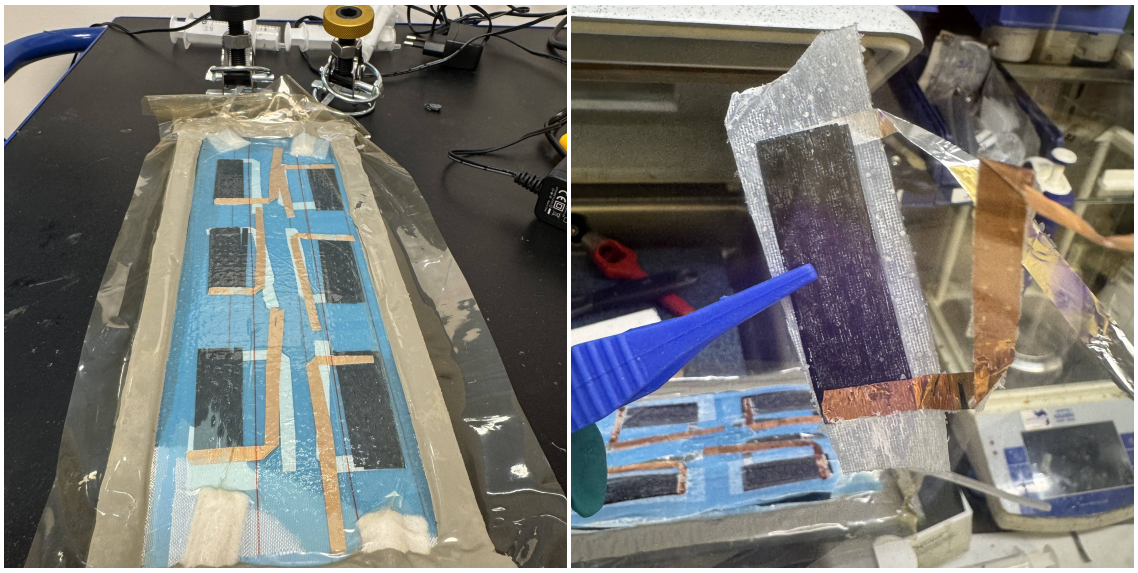

(a) **(b)**

Figure 3.5: (a) Infusion of a large vacuum bag using two outlets and two inlets, (b) cured cell from the larger vacuum bag infusion of stage 4.

As in stage 2 and 3, an additional 200 µL of electrolyte is added in the pouching, and EIS is performed before each cell is conditioned.

Table 3.1 provides an overview of the cells tested in Stage 1-4, and their sizes and stacking concepts. In the table, Stack concepts "Z" denotes a Z-stacking configuration, and the "#L" notation describes the number of layers, whereas in Cell ID, SL denotes "Single Layer" and DL "Double Layer".

Table 3.1: Testing protocol for cell concepts.

Cell ID	Stage	Size (mm)	Stack Concept	EIS Timing	No. Tested
DL	1	30×30	Z, 2L	After GCD	4
DL1_SLOW	1	30×30	Z, 2L	After GCD	1
SL1_SLOW	1	30×15	Z, 2L	After GCD	1
4L	1	30×15	Z, 4L	After GCD	1
DL_NMC	1	30×30	Z, 2L	After GCD	1
SL_NMC	1	30×30	1L	After GCD	1
DL_SLOW_R	2	60×15	Z, 2L	Before GCD	14
SL1	3	50×15	1L	Before GCD	4
DLP	3	50×15	Z, 2L	Before GCD	3
SLP_R	4	50×15	1L	Before GCD	16

3.2 Aircraft structures-design and manufacturing

3.2.1 Fuselage

The original aircraft fuselage is a balsa wood circular tube with a mass of approximately 12 g. However, this design is not suitable for the integration of structural batteries due to additional complexity of its circular geometry. Hence, the possibility of having a composite fuselage that can integrate structural batteries as a structural member as well as energy storage is explored. Since structural batteries are easier to integrate into flat surfaces, cross sections with only straight lines are studied.

A structural C-beam concept initially considered due to the simplicity in manufacturing had to be discarded due to the lack of torsional stiffness of open sections. Instead, a triangular beam concept is pursued and found promising. In this design three sides of the front section of the fuselage have structural batteries as part of the structure.

The fuselage is a triangular beam with a 25 mm equilateral triangle cross section in the front and tapers to a 10 mm equilateral triangle with the bottom side rounded out as shown in Figure 3.6.

(a) **(b)**

Figure 3.6: (a) Isometric view of the triangular fuselage, (b) side view of the triangular fuselage.

For future integration, it is intended that structural batteries should be integrated into the fuselage by embedding them into the 25 mm wide section of the fuselage. Individual structural batteries, each 50 mm long and 15 mm wide, can be grouped into segments. Within these segments, the structural batteries can be mechanically bonded together to improve load transfer capabilities and electrically connected in parallel to increase capacity. Three of these segments can be mechanically bonded to three sides of the triangular beam to form a section, and connected in parallel to further increase capacity. Three of these sections can run along the fuselage and can be electrically connected in series to match the voltage requirements of the motor. The idea is that this will result in a multifunctional component that simultaneously serves as a primary load-bearing structure and an energy storage device. This concept is illustrated in Figure 3.7.

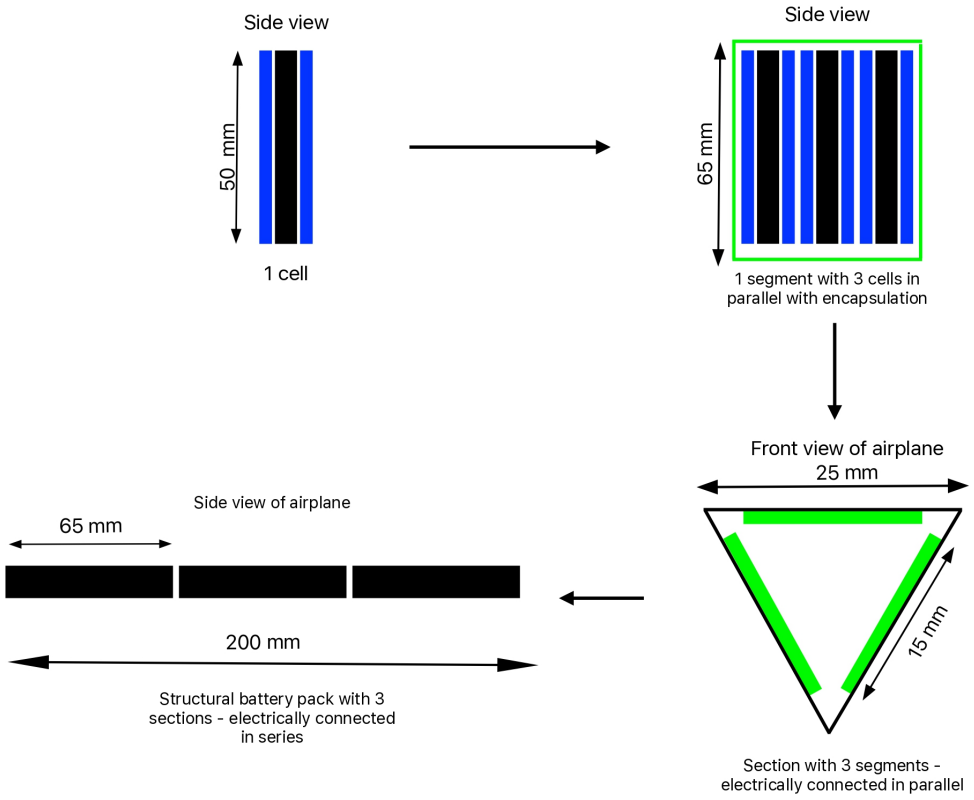

Figure 3.7: Visualisation of the structural battery pack concept with segments, sections, and the structural battery pack.

The fuselage is manufactured as a monocoque using two negative moulds, one for the 'V' section and one for the top face. The V-section negative mould is made using resin infusion on a 3D-printed pattern using Textreme® spread tow plain weave carbon fibre [28] and NM693 Infusion Epoxy [29] followed by post curing at 150 °C for 4 hours to raise the glass transition temperature of the epoxy to 168 °C. Manufacturing of these parts can be seen in Figure 3.9.

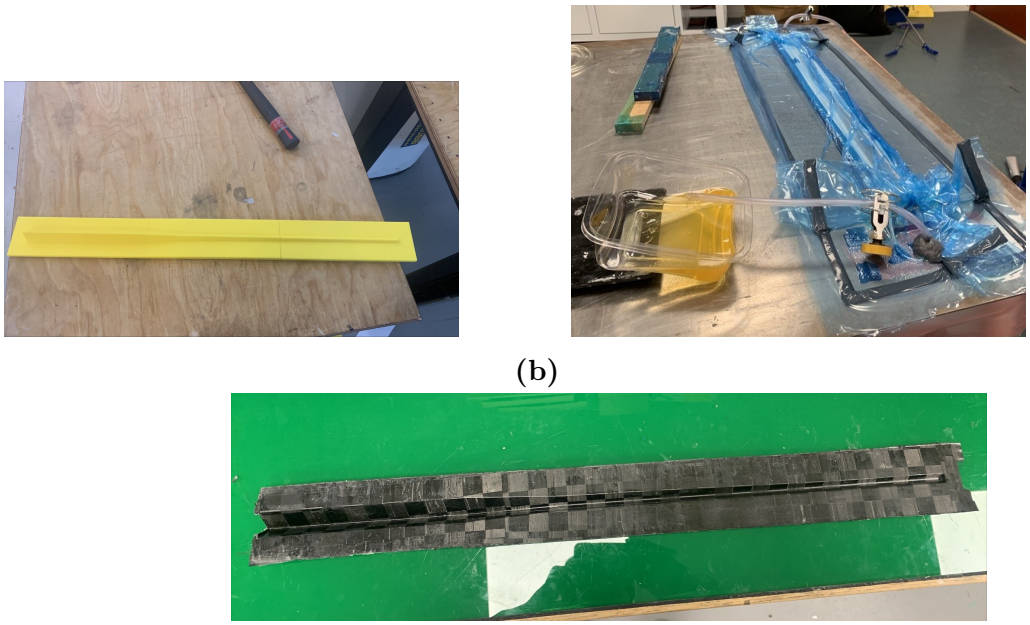

Figure 3.8: (a) Pattern 3D printed in PLA, (b) resin infusion, (c) and cured negative mould of the V-section.

A flexible carbon fibre sheet is used as the negative mould for the top face, as the top face is pre-dominantly flat with some slopes. The material used in the fuselage is VTC401-C94G-PW-HS-1K-48%RW [30], which is a high strength 1K plain weave carbon fibre prepreg. A layup of $[\pm 45_2]$ is used throughout the fuselage, except at the front section where structural battery integration happens, where a layer of cellulose separator is added on the inside to isolate the conductive carbon fibre skin from the structural batteries and prevent leakage currents.

The fibres are initially laid up on the V-section. A self releasing tubular bag is placed in the hollow section, followed by closing the carbon fibre triangular loop. The flexible plate is then placed on top and an envelop vacuum bag is made that interfaces with the tubular bagging film inside. This ensures that there is consolidation on all three sides and corners when the autoclave applies an overpressure of 6 bar.

3.2.2 Wingbox

The wingbox is designed to be aerodynamic and light while providing enough strength to withstand load transfer from the wings. The MB253515 aerofoil [31] appears as a suitable candidate due to its low drag characteristics at the aircraft's operating reynolds number ranges. The wingbox has a chord of 130 mm and span of 10 mm along with a 5° draft angle on the side faces as shown in Figure 3.9a to facilitate manufacturing. A layup of $[\pm 45]$ with local $[\pm 45]$ reinforcements at the wing spar attachment points is used.

(a) **(b)**

Figure 3.9: (a) CAD model of the wingbox mould, (b) 3D printed mould wrapped in PTFE tape for release properties.

3.2.3 Motor attachment

The motor is attached to the front of the fuselage and has mounting holes corresponding to the motor design as shown in Figure 3.10. The attachment also acts as a front bulkhead for the fuselage and protects internal components in the event of a crash. A layup of $[(0/90)_2]$ is used and the attachment is glued to the fuselage using Loctite 401.

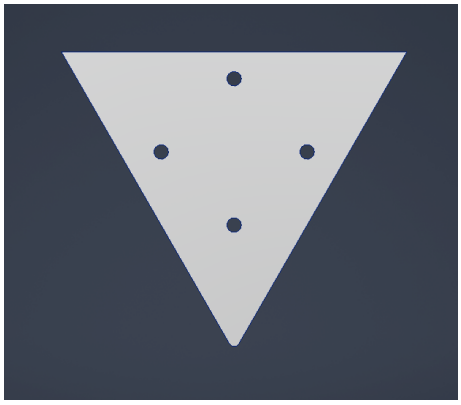

Figure 3.10: Sketch of the motor attachment/front bulkhead in CAD.

3.2.4 Stabiliser attachments

The vertical and horizontal stabiliser attachments are made to be as light as possible while being capable of withstanding the shear and bending loads produced due to the tension in the rubber band which attaches to it.

A flat double hook structure as shown in Figure 3.11 is made using the 1K plain weave prepreg and Divinycell H60 foam core [32] with a [(±45)/1mm H60 core/(±45)] layup. The ±45 plies provide the shear strength while the sandwich structure enhances bending stiffness of the part. It is mounted to the fuselage by gluing the middle section using Loctite 401.

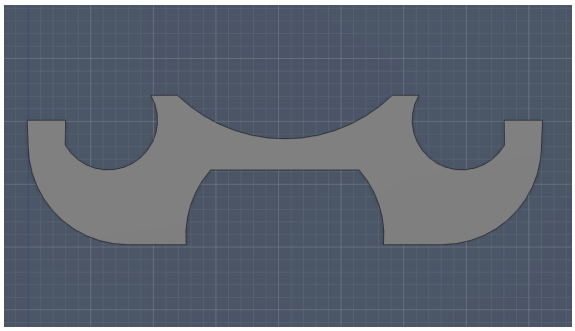

Figure 3.11: Sketch of the double hook stabiliser attachment.

3.3 Propeller and motor selection

Due to the broad use of BLDC in RC applications, and its small size and high efficiency, it is chosen as the preferred motor. The motor, along with a small ESC is purchased off the shelf. Low weight is of the highest priority, but an unreasonably high KV-rating will not play to the advantage of the system efficiency, as such motors are made for quadcopters and not fixed wing aircrafts. Hence, the lightest available BLDC motor for fixed wing applications was chosen, the T-HOBBY AM20 F3P Airplane Brushless Motor, which has a KV rating of 1500, and a mass equivalent to the rubber motor it replaces, of 10 g. Based on the benchmark tests from the supplier, this motor provides a better thrust with the same power [23], [33]. The AM20 BLDC Motor has a 2s LiPo rating, which is equivalent to 8.23 V in the suppliers benchmark tests. This means that a 3s configuration of structural batteries is necessary, providing 8.4 V of nominal voltage in the pack.

In order to select a suitable propeller for the application, the thrust requirements from the aircraft is modelled using a python script. The wing has a span of 800 mm and a chord of 105 mm. The aerofoil used in the wing provided by Elitkomposit was not identified, but work done by Michael Selig et al. on Free Flight aircraft aerofoils [31] indicates that the L/D ratio of these aerofoils at operational angles of attack is approximately 20. To account for parasitic drag caused by the propeller, fuselage, and the stabilisers, the estimated L/D for the calculations is reduced to 19.

Assuming a conservative final weight of 100 g for the aircraft, it is found that a thrust force of 5.3 g is required to maintain the aircraft at cruise. From Equation 2.12, the velocity of the aircraft at cruise is calculated as 6 ms^{-1}.

The UIUC Propeller Database [34] maintained by the University of Illinois at Urbana-Champaign (UIUC) contains wind tunnel measurements for approximately 70 small scale propellers, with the recorded data including coefficients of thrust, power, and torque for these propellers at a wide range of advance ratios and speeds. Calculations done for multiple propellers using Equations 2.16 and 2.18 imply the DA4052 5x4.92(+5 deg) as the best candidate since it provides a thrust of 5.37 g at 3800 rpm at a forward velocity of 6 ms^{-1}. APC Freeflight 4.2x4 [35] is found to

be the best off the shelf propeller.

3.4 Propeller design, manufacturing and testing

Since DA4052 5x4.92(+5 deg) is not a commercially available propeller [36], a 3D model of the propeller is made using the geometry data available in the UIUC database as shown in Figure 3.12.

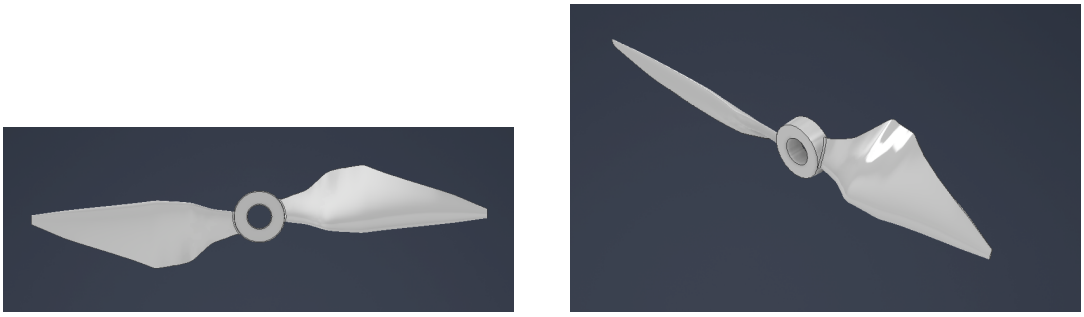

(a) **(b)**

Figure 3.12: (a) Front view of propeller in CAD, (b) isometric view of the propeller in CAD.

Sample propellers as shown in Figure 3.13 made using Fused Deposition Modeling (FDM) and Selective Laser Sintering (SLS) 3D printing does not provide satisfactory leading and trailing edges. They also have a mass of approximately 4 g, which is excessive for a propeller of this size.

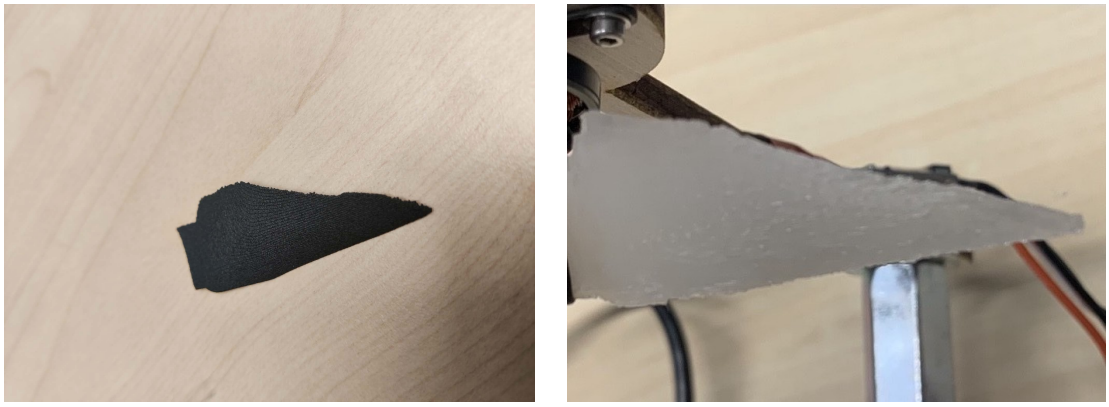

(a) **(b)**

Figure 3.13: (a) SLS 3D printed blade, (b) FDM 3D printed blade.

Therefore, it is decided to make the propeller out of carbon fibre composite. Figure 3.14 shows the CAD model of the mould and the final milled mould. Conventionally, composite propellers are made using a 2-part mould, but since the cross section of the blade is very thin, it is decided to only make one mould using

the suction side of the blade and let the thickness of the composite layup form the pressure side.

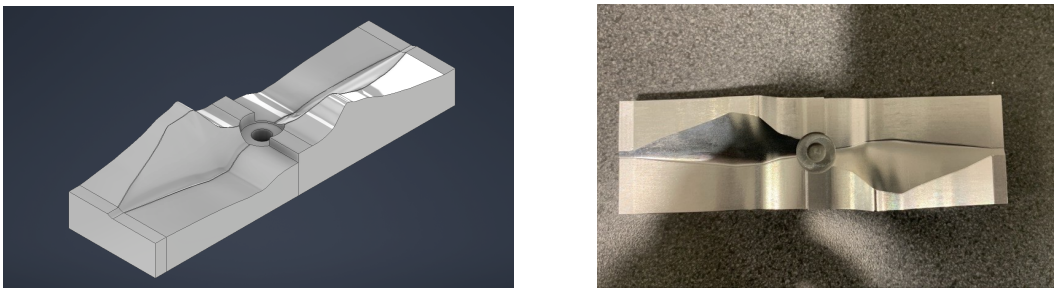

(a) **(b)**

Figure 3.14: (a) CAD model of propeller mould, (b) mould milled in Al6061-T6.

A central insert 3D printed out of PC Blend HT LCF [37] from add:north filaments as shown in Figure 3.15 acts as both the propeller hub and as an integrated core extension into the blade root region.

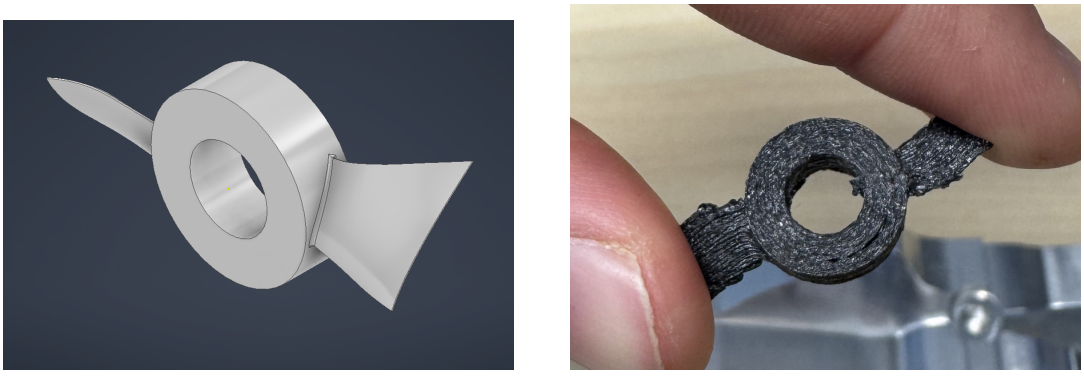

(a) **(b)**

Figure 3.15: (a) CAD of propeller hub insert, (b) 3D printed propeller hub insert.

A layup of $[(\pm 45)/(0/90)/(\pm 45)]$ is used, with the first layer underneath the hub insert acting as the bottom skin, the second layer flush with the hub insert, and the final layer as the top skin of the hub root as shown in Figure 3.16. Due to geometrical inaccuracies in 3D printing, some local reinforcements are added at the blade root region to provide support to the hub during autoclave curing.

Figure 3.16: Layup of propeller skin – left blade has the bottom skin only, while right blade has the bottom and middle layers.

A static thrust measurement set-up is built in-house to test the thrust of various propellers in static conditions and compare them with the UIUC Propeller Database measurements. The setup involves making a lifted mounting bracket for the motor and propeller with a transparent base plate as shown in Figure 3.17. Thrust is measured in g by keeping the setup on top of a weighing scale and running the motor and propeller using a AIM TTI PL303QMD power supply, which also measures the current drawn by the motor. The speed of the propeller is measured using a Lutron DT-2249 Digital Stroboscope, and thrust is measured using a KERN PLS weighing scale for a wide range of speeds and throttle percentages. This test rig has some sources of inaccuracies like the motor mounting member disturbing the airflow behind the propeller and the extra up force created due to the pressure difference between the suction area (the area between the motor mount and base plate) and the region underneath the base plate. But these errors were deemed to be of acceptable amounts since the goal of the study is to compare different propellers to each other and to the UIUC calculated values and to derive realistic values of current drawn by the motor during flight.

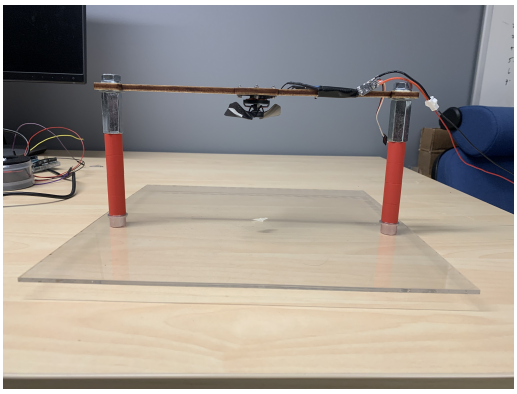

(a)

(b)

Figure 3.17: (a) Propeller test rig, (b) propeller test rig in action with the stroboscope and weighing machine.

3.5 Electrical topology and design

After propeller and motor testing have provided an estimated current requirement, the electrical topology, including the battery pack design, can be determined. To maintain a low weight, and a good fit into the fuselage, a compromise has to be found between maintaining a decent discharge rate, while keeping the manufacturing effort at a reasonable level, and simplifying cell integration and pack complexity.

In order to control the chosen 3-phase BLDC motor, a recommended ESC is chosen commercially. The T-HOBBY AM16A is chosen due to its low mass of 1.1 g and suitability for the 8.4 V system. However, implementation of the ESC means that the system needs additional functions to work. Firstly, the inverter of the ESC has a high capacitive load, leading to a high inrush current during start-up. Hence, a pre-charge is necessary, in order to not put a too high load on the cells.

The pre-charge design is evaluated in Analog Devices free circuit simulation tool LTSpice, and uses a P-channel MOSFET and a capacitor between gate and source, which causes the gate voltage to slowly move from the resistive area into a steady state voltage determined by how the two resistors are chosen. The final design can be seen in Figure 3.18.

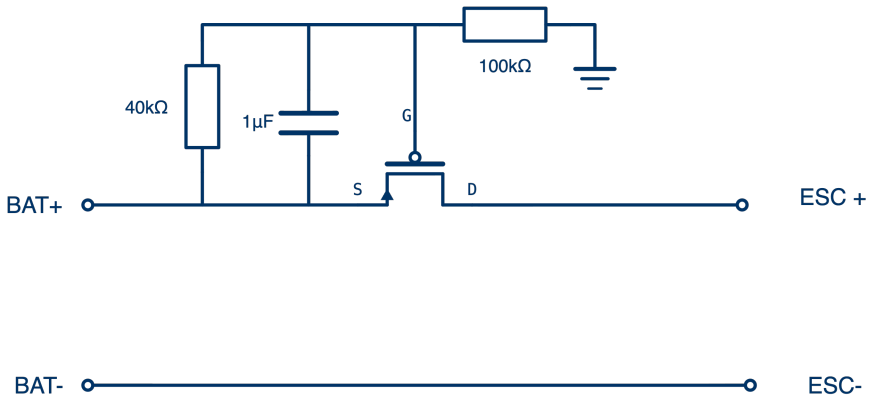

Figure 3.18: Circuit schematic of the transistor-based pre-charge used when starting the ESC.

Secondly, the ESC itself needs instructions on how the motor should be controlled. In order to start the motor, the ESC firstly needs to arm, which means a 1000 µs pulse is sent at 50 Hz. When this procedure is completed, a longer pulse is sent to start the motor. This pulse can be between 1000 µs and 2000 µs depending on the desired speed [38]. This procedure is validated using an Arduino and the servo library to calibrate the ESC and test the desired power sequence of the system. However, an Arduino is not suitable to have on the aircraft, due to its large size and weight, its high current use, and the fact that it is oversized in terms of computational complexity. Hence, the same processor used for the torch demonstrator, an ATMega328PB, is used for this purpose. The ATMega also supports hardware PWM, meaning that the PWM signal is configured into the hardware, and then runs continuously without any intervention from the software. The ATMega328PB operates using 5 V logic, which means that it can be powered from the BEC system of the ESC [39].

After ensuring that the motor can be properly operated, it now needs to be confirmed that the cells can be protected and that the motor is turned off when the pack voltage is too low. As the system has a 3-series cell configuration, voltage monitoring of the pack alone is not sufficient. Each cell group connected in series, needs its own monitoring. This monitoring can also be performed using the ATMega processor. However, as the ATMega runs on 5 V, these measurements have to be voltage divided to below 5 V in order to not break the processor. By using 10 kΩ and 27 kΩ resistor, the voltage can be scaled down by 2.74 times, and hence go from a maximum of

$$3.55\ \text{V} \cdot 3 = 10.65\ \text{V} \Rightarrow \frac{10.65}{2.74} = 3.95\ \text{V} \tag{3.1}$$

which brings down the voltage well below the critical 5 V. This final configuration is illustrated in Figure 3.19, where U_{pack} connects the ATMega to the voltage divided full pack voltage, U_{CELL2} the lower two cell groups, and U_{CELL3} monitors the bottom group. The full cell voltages are connected to the corresponding TestPoints (TP).

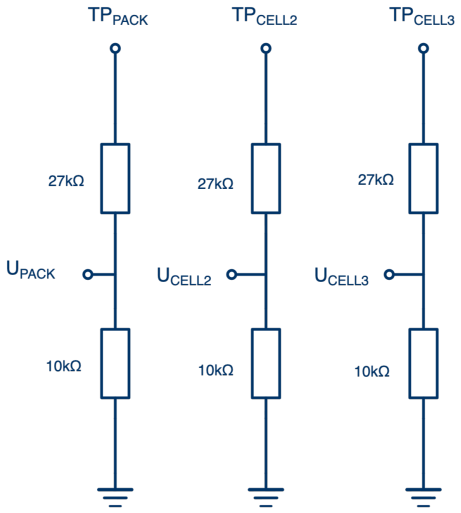

Figure 3.19: Voltage division for cell monitoring, where TP indicates where each cell is connected, and U_{PACK}, U_{CELL2} and U_{CELL3} are the nodes at which the ATMega measures the voltage.

The ATMega can then be programmed to cut-off when any of the cells reaches their critical lower voltage cut-off limit, and if a testbench flight is made, a UART-connection can be made to the processor to plot and view how the voltages change during operation.

In conclusion, a separate custom designed circuit board, which handles pre-charging, cell monitoring, and low-voltage cut-off, can in combination with the ESC and BLDC Motor handle all electrical system functions on-board the aircraft. However, during charging, simple monitoring is not sufficient. If one cell group were to be fully charged before the others, the charging must be by-passed to allow the other cells to fully charge. The most simple set-up is chosen, which is to simply perform passive balancing during charging, using the Texas Instruments BMS evaluation board BQ76942EVM. This evaluation board, provides a computer interface to monitor and log the charging process of the battery pack if desired [40].

Finally, as the Texas Instruments Module provides no control of charging current or voltage, a 230 VAC to 12 VDC Wall connector is used, and connected to a programmable DC-DC converter, to more conveniently control the charging of the aircraft. Using an upper current limit and a set voltage, a CC-CV charging of the cells can be performed.

The final electrical system topology is summarized in Figure 3.20, with the system separated into external charging circuit and on-board system.

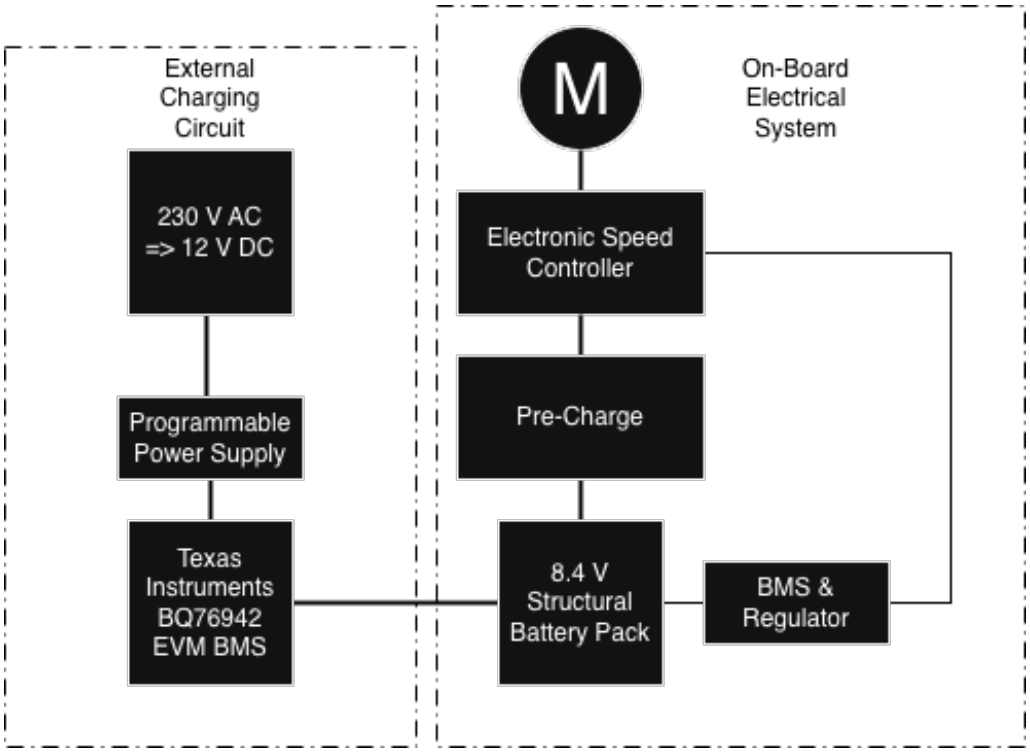

Figure 3.20: Illustration of the complete electrical topology for the aircraft.

4
Results and Discussion

The following chapter describes and analyses the results of the cell evaluation and manufacturing, and the electrical and mechanical system design.

4.1 Cell performance

The following section describes the results from each cell manufacturing stage, and discusses the key takeaways.

4.1.1 Results from stage 1

NMC-foils are used both as single layer and double layer cells. Notably, the NMC-foils used as an alternative positive electrode do not activate in the SBE system, which means that this approach can quickly be abandoned.

The double layer cell, with a z-stacked separator and a PE-NE-NE-PE configuration, proves to be the simplest to produce, as the separator keeps the negative electrode safely wrapped and protected from short circuits. This also minimises the problems from static electricity caused by the cellulose separator. With this method, stacked cells can be manufactured with a good success rate.

DL2 exemplifies the best performance from this configuration, with a GCD capacity of 7.5 mAh, and a CC-CV charge capacity of 8.3 mAh. Based on the GCD capacity, this gives an energy density of 29.9 Whkg^{-1}. The data for DL2 is presented in Table 4.1.

Table 4.1: Performance of a double layered z-stacked cell.

Cell ID	C/20 GCD Capacity (mAh)	Mass (mg)	Energy Density (Wh kg^{-1})
DL2	7.5	702	29.9

The full CC-CV charging of DL2 can be seen in Figure 4.1.

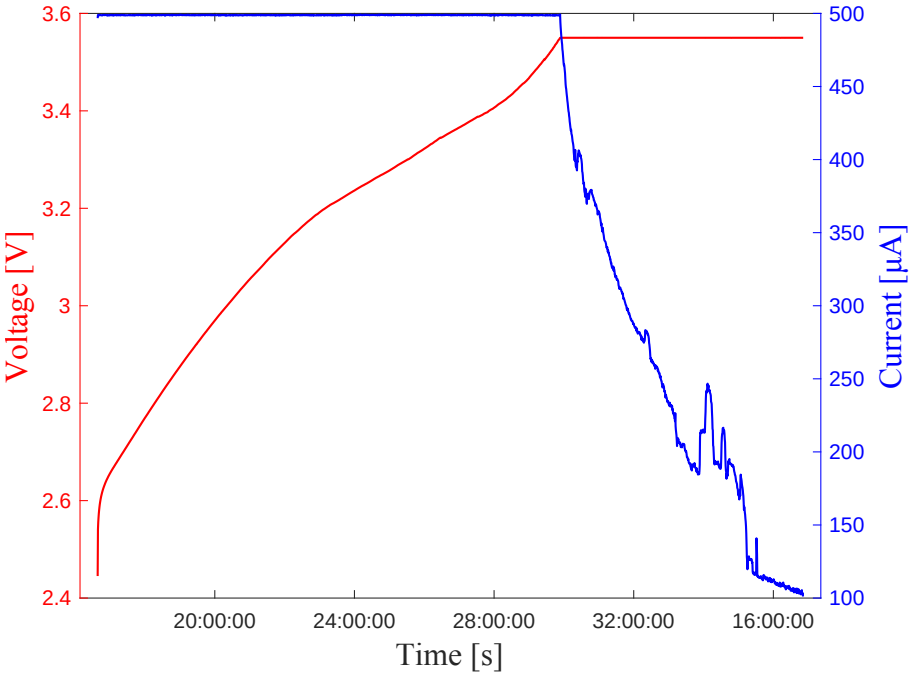

Figure 4.1: CC-CV charging procedure of DL2.

This shows that z-stacked cells are capable of delivering good electrochemical performance. The stacked cell and single layered cell with a dwell time before curing proves to give a very good capacity after conditioning. The GCD at C/20 after ten cycles is given in Table 4.2, along with the cells mass and energy density.

Table 4.2: Performance of cells fabricated with dwell time.

Cell ID	C/20 GCD Capacity (mAh)	Mass (mg)	Energy Density (Wh kg^{-1})
DL1_Slow	6.4	683	26.2
SL1_Slow	2.3	263	24.5

These cells also prove to have the best impedance, with very low charge transfer resistance R_{ct} and ohmic resistance R_{Ω} after conditioning. The DL1_SLOW cell shows three semi-circles, which makes it more difficult to find the EECM. The impedance spectra is seen in Figure 4.2.

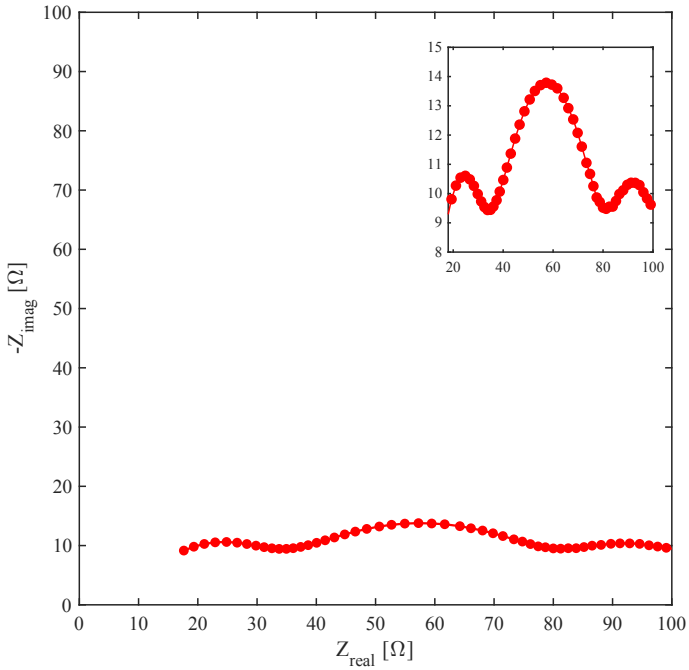

Figure 4.2: EIS from double layered cell with dwell time.

The low resistance values are of great importance when optimising for power, as the IR-drop can be reduced significantly. This, along with the consistency in terms of performance between the two cells with a dwell time, makes it a suitable candidate for the aircraft.

However, extending the stack to a four layer configuration proves to come at a cost of impedance, although cycling ten GCD cycles successfully. The GCD cycling of the four layered z-stacked cell along with its impedance spectra after cycling is seen in Figure 4.3.

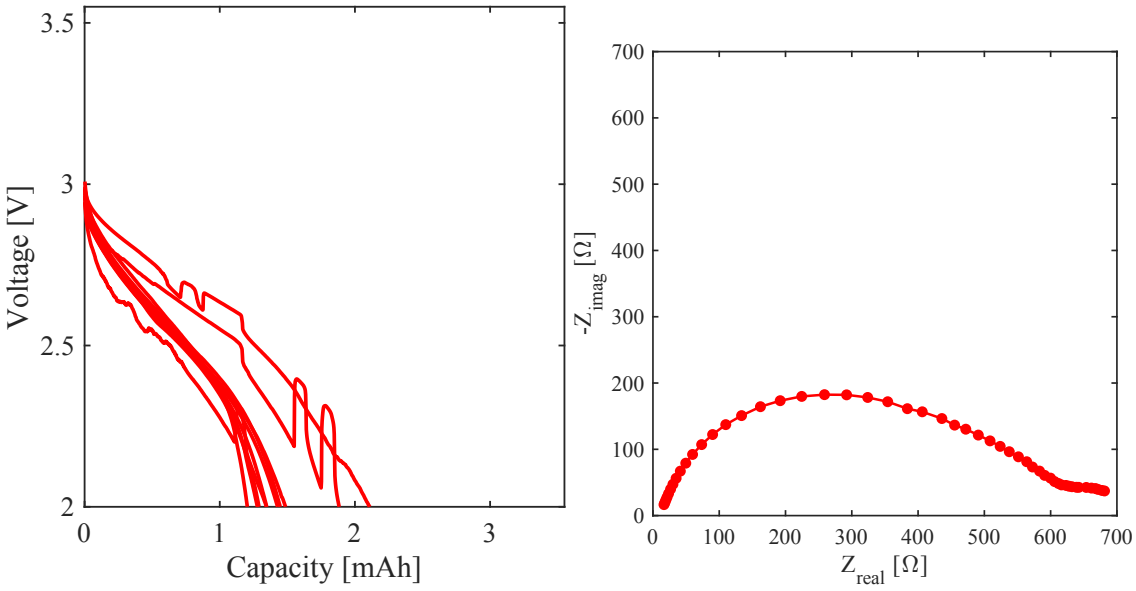

(a) **(b)**

Figure 4.3: (a) GCD discharge capacity of the four-layered cell during the ten conditioning cycles, with significant IR drops due to the high impedance, (b) impedance of a four layered z-stacked structural battery, indicating that further increase of layers comes with a cost in terms of impedance.

In Figure 4.3, it is clear that the impedance growth is causing significant IR-drops when charging and discharging, affecting the usable capacity. Table 4.3 shows the key results, indicating that the capacity and subsequently the energy density are inadequate. Notably, a slower CC-CV charging allows a charge capacity of up to 3.5 mAh, which confirms that the usable capacity is primarily limited by the IR drop. However, these slow discharge conditions are not to be expected in an aircraft application. Hence, the double layered cell with dwell time is selected for use in a repeatability test, as this topology provides better high power suitability.

Table 4.3: Performance of four-layered z-stacked cell.

Cell ID	C/20 GCD Capacity (mAh)	Cell Mass (mg)	Energy Density (Wh kg^{-1})
4L	1.5	916	4.6

However, it should be noted that the lower reported energy density in Table 4.3 is likely also affected by a more difficult manufacturing process. The small electrodes and the repeatable folded cellulose likely cause a higher cellulose parasitic weight, and non-ideal alignment of the electrodes.

4.1.2 Results from stage 2

Stage 2 proceeds with the z-stacked layout including a dwell time but a revised dimension of 15x60 mm. DL_SLOW_R2, DL_SLOW_R8 and DL_SLOW_R9

exemplify the general performance of the cells and their first ten cycle discharge capacities along with their EIS spectra before cycling are presented in Figure 4.4.

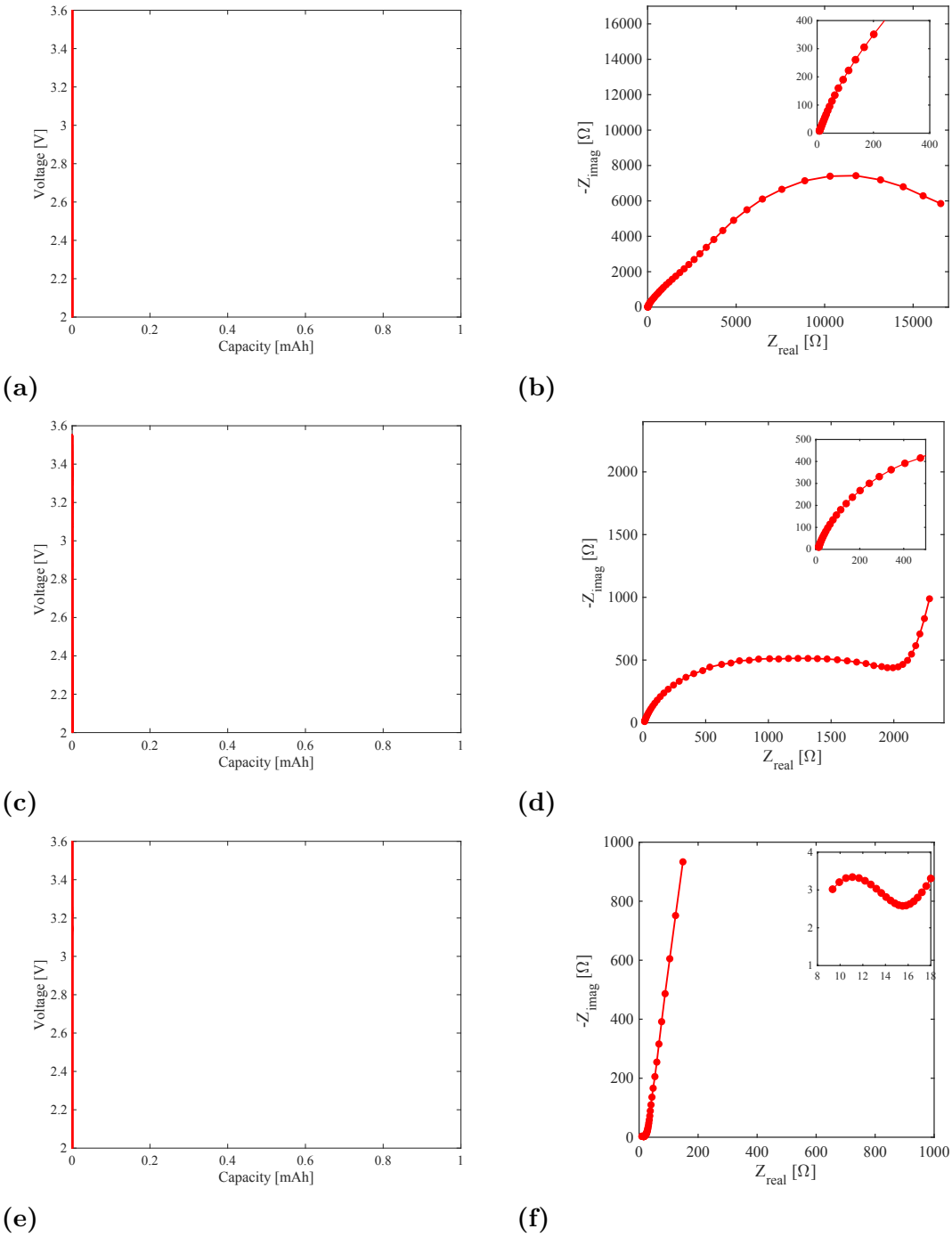

Figure 4.4: (a) The cycling discharge capacity of DL_SLOW_R2 over the first ten cycles, (b) the impedance for DL_SLOW_R2 before conditioning, (c) the cycling discharge capacity of DL_SLOW_R8 over the first ten cycles, (d) the impedance for DL_SLOW_R8 before conditioning, (e) the cycling discharge capacity of DL_SLOW_R9 over the first ten cycles, (f) the impedance for DL_SLOW_R9 before conditioning.

The first cycle failure, which leads to ten GCD cycles being performed instantaneously, was first thought to be related to the very high R_{ct} values notable for the cells in Figure 4.4b, 4.4d, and 4.4f. Hence, two cells are manufactured using a negative electrode which extends outside of the positive electrode, to improve SBE wetting. Similarly, another cell with the similar failure mechanism, is altered and has its positive electrode narrowed. Its cycling performance before and after this modification, along with its impedance spectra before and after the modification, is shown in Figure 4.5.

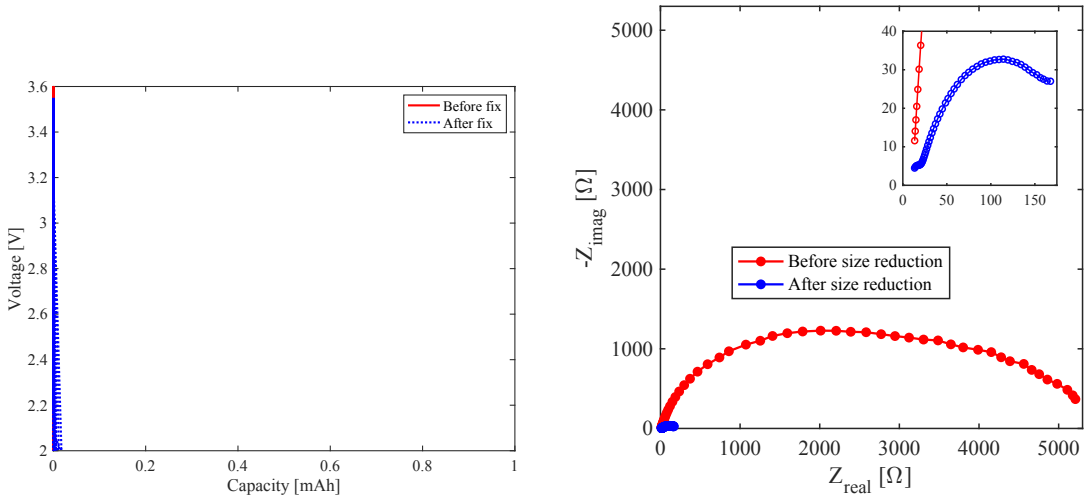

(a) **(b)**

Figure 4.5: (a) Capacity of DL_SLOW_R3 before and after positive electrode size reduction show that improvement is negligible on a µAh scale, (b) impedance change after positive electrode size reduction.

The original topology significantly impairs carbon fibre wetting. However, addressing it with a positive electrode which is reduced in its size does not restore stable cycling behaviour, as the discharge capacity is within a negligible magnitude, although it significantly improves R_{ct}. Hence, the cell design for an aircraft needs a design revision.

4.1.3 Results from stage 3

For stage 3, the problem of fibre wetting is further addressed by including pinholes in the positive electrodes. Additionally are the positive electrodes reduced in size compared to the negative electrode, with a positive electrode size of 40x15 mm and a NE size of 50x15 mm. Figure 4.6 shows the EIS of selected cells, with DLP1, DLP2 and DLP3 being double layered cells, and SLP2 and SLP3 being single layer cells. Although the impedance values show greater consistency among the cells, the cycling performance proves inadequate, with only a single double layered cell and a single layered cell successfully cycling ten cycles and subsequent full CC-CV charge.

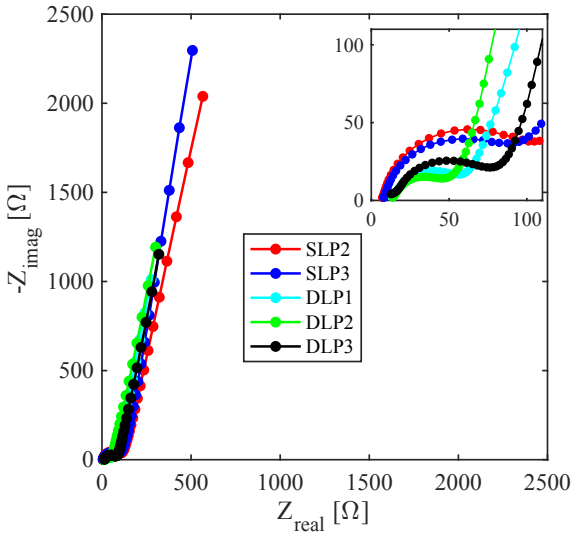

Figure 4.6: Impedance of selected double layered and single layered cells from stage 3 before conditioning.

With a larger total electrode area, the double layer cells show an improved R_{ct} and a reduced Warburg impedance tail. However, activation and cycling of these cells are less successful, with only DLP1 successfully cycling. This indicates that an encapsulation effect from the aluminium foil still occurs, and that there is a problem with mass transport. A simplified single layered layout is chosen for stage 4 repeatability tests to minimize complexity.

4.1.4 Results from stage 4

Stage 4 proceeds with a simplified single layer layout to avoid further complexity and failures. Pinholes in the positive electrodes are kept, and a larger negative electrode is also manufactured to maximize the SBE wetting. SLP_R2, SLP_R3, and SLP_R7 exemplifies the performance of the cells manufactured in this stage, and their GCD cycling of ten cycles and impedance before cycling can be seen in Figure 4.7.

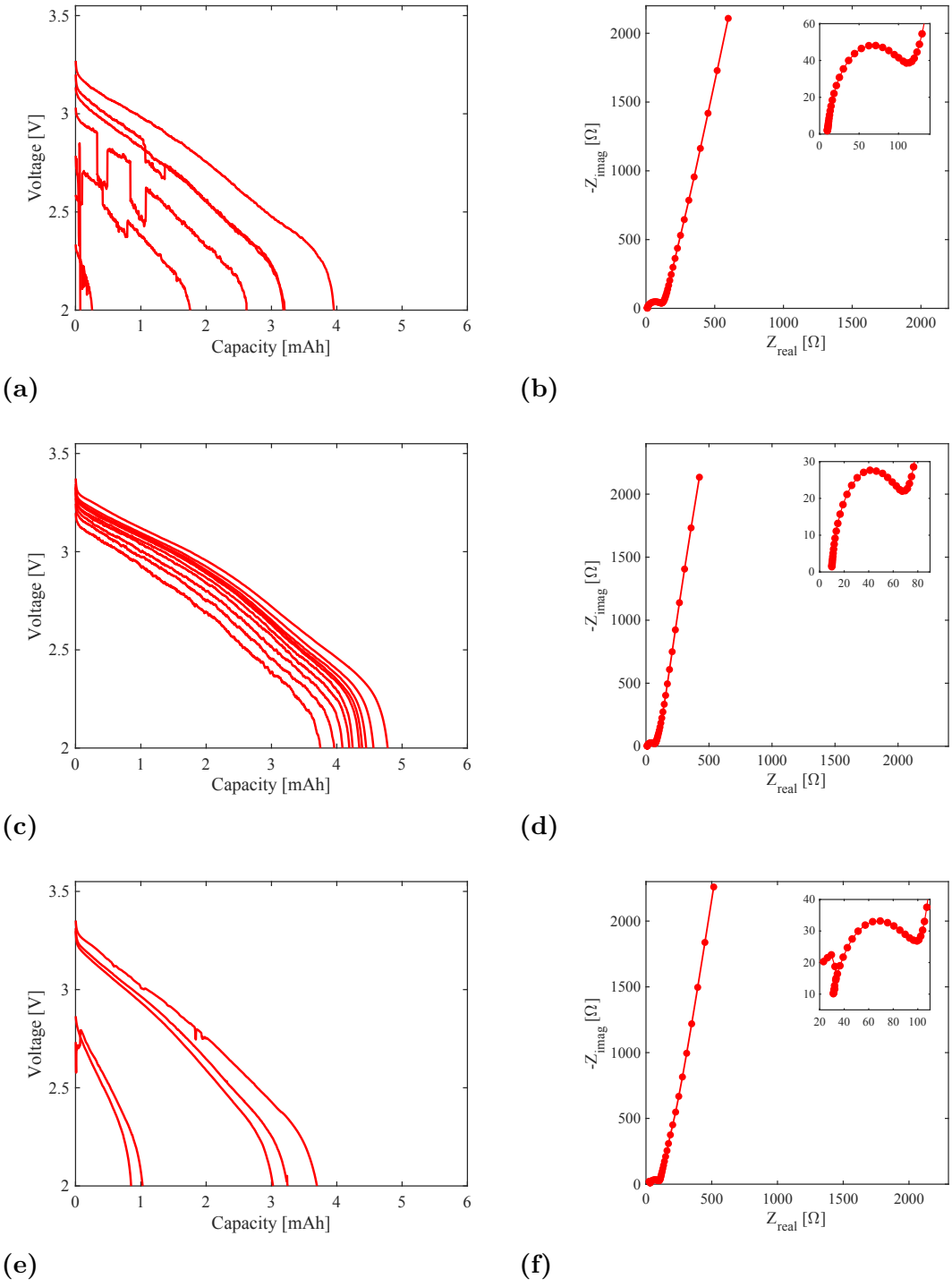

Figure 4.7: (a) GCD cycling discharge capacity of SLP_R2, (b) impedance of SLP_R2, (c) GCD cycling discharge capacity of SLP_R3, (d) impedance of SLP_R3, (e) GCD cycling discharge capacity of SLP_R7, (f) impedance of SLP_R7.

Although a great consistency improvement is seen in terms of impedance, only two out of 18 cells successfully cycles the ten cycles of conditioning, one of which is the SLP_R3 seen in Figure 4.7c. Hence, EIS as a characterisation method does not give any indication whether a cell will work. However, more than 50% of all

cells successfully activate and cycle one full charge-discharge cycle before failing. A visual inspection is conducted of one of the failed SLP_R cells to investigate why the failure reliably occurs for a majority of the cells. The opened cell can be seen in Figure 4.8.

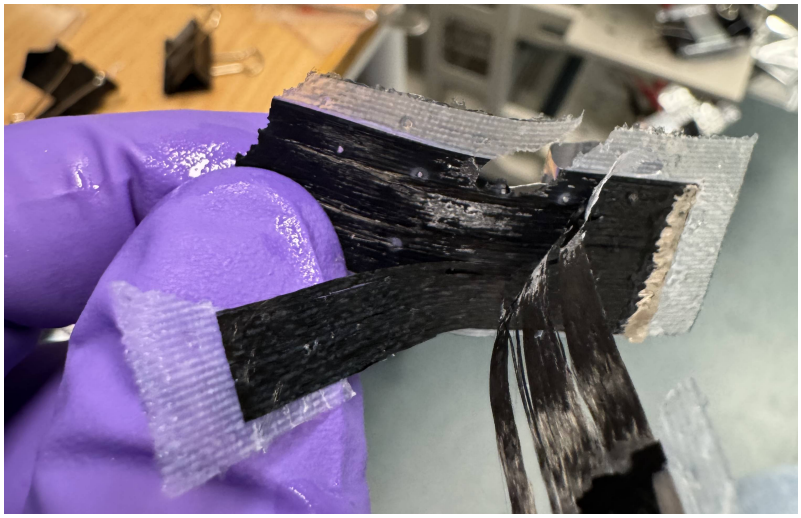

Figure 4.8: Photograph of opened from stage 4, shows a cured but dry negative electrode.

Figure 4.8 indicates that the fibres of the negative electrodes are cured but dry, with few signs of electrolyte. This is very likely to cause mass transportation problems that lead to the spiking behaviour seen in the cycler.

The insufficient wetting may be explained by the fact that the cellulose separator is thinner and less porous than the Whatman separator used in the first-generation structural battery cells, leaving less free volume for SBE uptake and slower resin penetration. In the all-fibre structural battery, which uses the cellulose separator, the carbon fibre positive electrode provides additional internal surface area and pore space that can absorb and distribute the SBE, which is not available in the present first-generation configuration. As a result, the present cell design may experience incomplete impregnation and insufficient SBE matrix formation, leading to early failure after initial activation and cycling.

For the reason described above, it is concluded that the next generation of structural batteries, the all-fibre battery, should be used in the demonstrator, to provide a more robust cell architecture.

4.2 Aircraft structural design

The various manufactured components are pictured in Figure 4.9 and a bill of materials (BOM) of all in-house manufactured aircraft structures in Table 4.4.

(a)

(b)

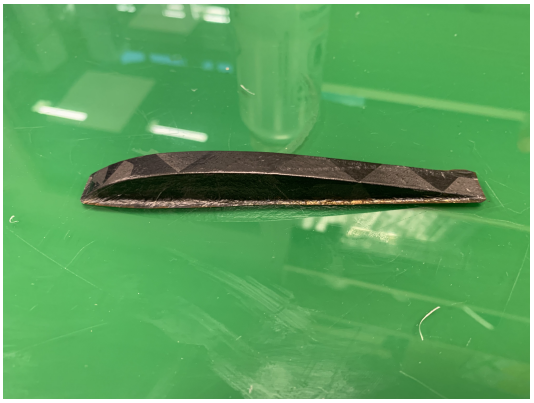

(c)

(d)

(e)

Figure 4.9: Manufactured (a) propeller, (b) fuselage, (c) wingbox, and (d) stabiliser mounts, (e) motor attachment.

Table 4.4: BOM of all in-house manufactured structures.

Part Name	No. of Units	Mass per Unit (g)	Total Mass (g)
Propeller	1	1.692	1.692
Fuselage	1	11.151	11.151
Wingbox	1	1.196	1.196
Horizontal Stabiliser Mount	2	0.050	0.100
Vertical Stabiliser Mount	2	0.050	0.100
Motor Attachment	1	0.100	0.100
Total			**14.339**

Information about all bought parts and parts donated by Erik Kullgren from Elitkomposit can be found in Appendix A.

4.3 Propulsion system design

The electrical topology in its entirety can be viewed in Figure 3.20. The custom components — regulator, bulk capacitors, pre-charge circuit, and cell monitoring — are gathered onto one PCB.

4.3.1 PCB evaluation

Figure 4.10 shows the final PCB and where each function is handled.

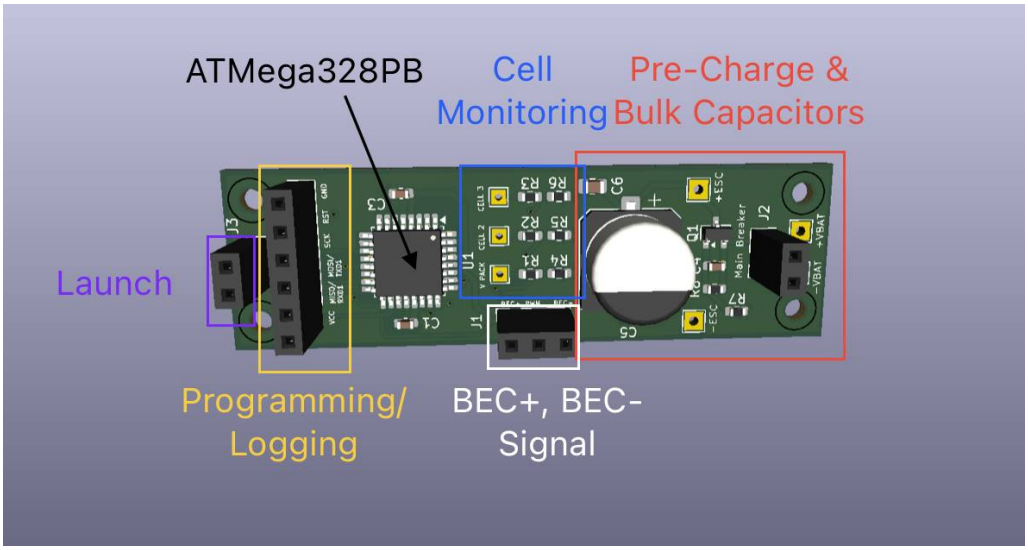

Figure 4.10: PCB overview with all implemented functions.

The pre-charge, located right by the pin socket for the main switch, which limits the current from the batteries to the speed controller and the bulk capacitors when the main breaker is turned on, is evaluated by measuring the inrush current before and after implementation. Figure 4.11 shows the difference using a power supply as the power source.

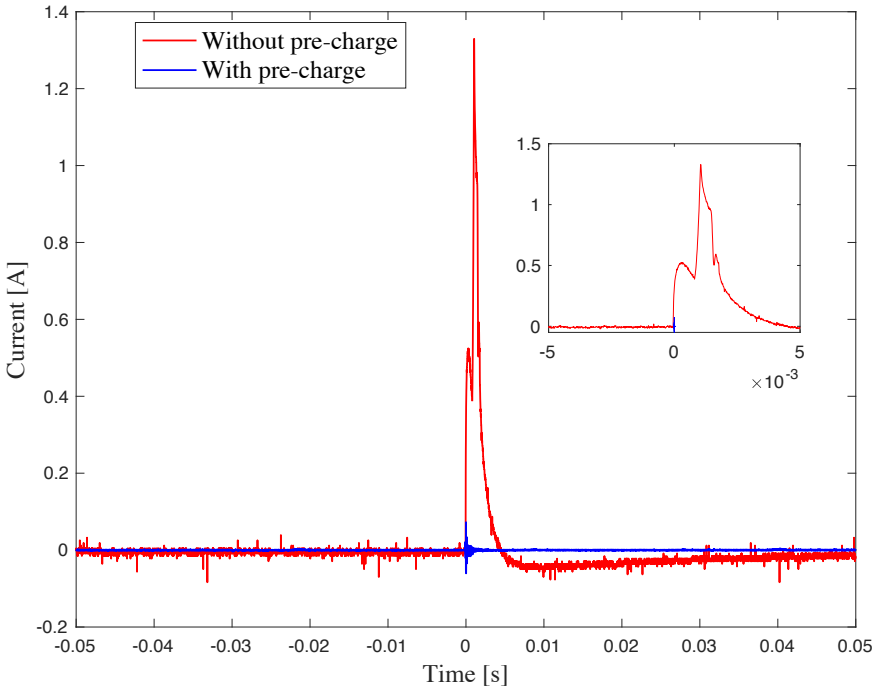

Figure 4.11: ESC start-up current before and after pre-charge implementation.

This confirms the need for the pre-charge circuit, and that the reduction is significant and can reduce the load of the cells when capacitors on the speed controller and PCB are being charged.

To verify that the ATMega provides a correct speed signal to the ESC, measurements were taken both before and after the ESC start-up. These measurements were then compared to the pulse widths recorded for various throttle settings when the ESC was driven by the Arduino. The reference measurements from the Arduino for selected throttle signals are presented in figure 4.12.

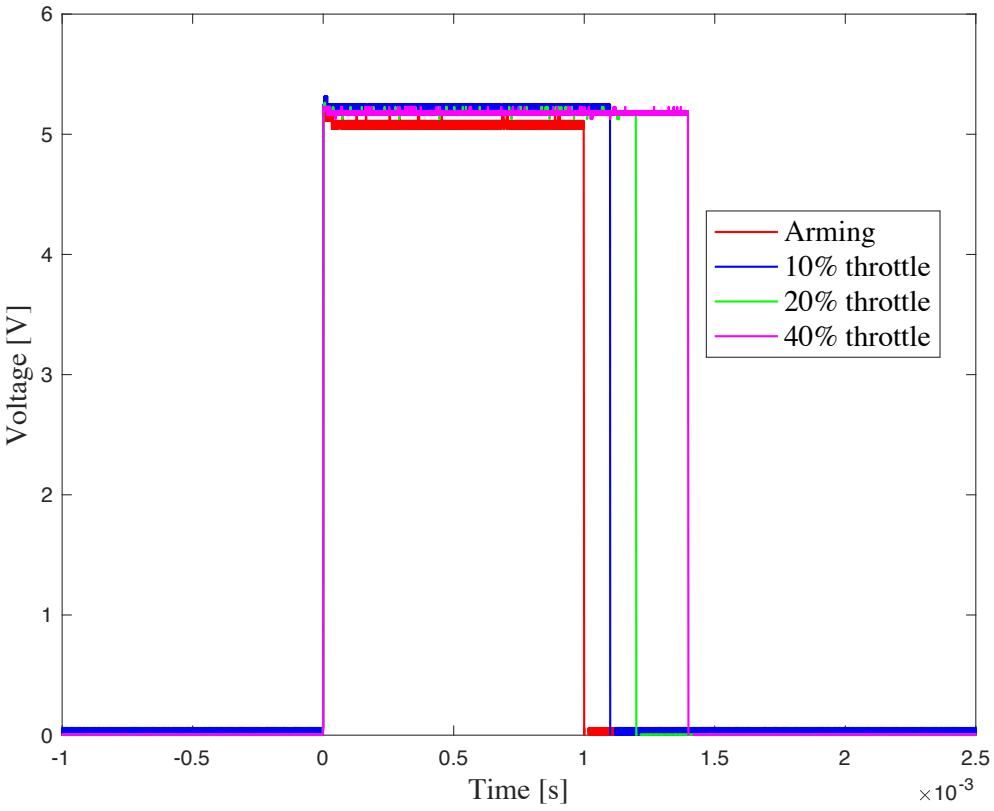

Figure 4.12: Oscilloscope measurements from the Arduino speed signal for different throttle signals.

Since the ATMega on the PCB behaves identically to the Arduino benchmark during start-up, and the pulse widths observed on the oscilloscope are the same, it can be concluded that the ATMega is capable of reliably starting the aircraft propeller. Furthermore, the transition from arming to start-up has been verified to work correctly using the launch signal button.

The cell monitoring is tested using a cell simulator of three 10 kΩ resistors connected in series on a breadboard. By connecting a monitoring cable to each resistor, the cell voltage is measured of each simulated cell. The monitoring is tested with a power supply where the voltage is slowly decreased. The measured voltages can be seen in Figure 4.13.

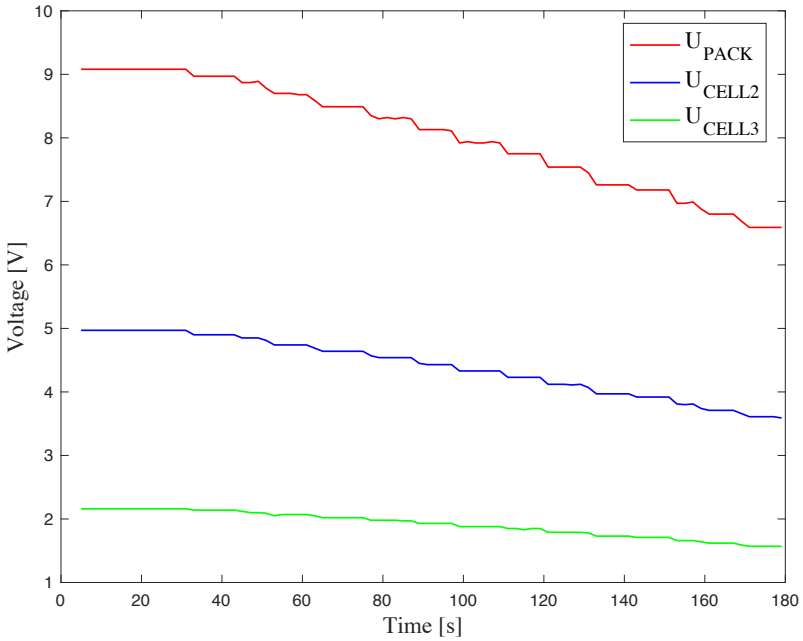

Figure 4.13: Voltage monitored by ATMega328PB in cell simulator circuit.

Notably, this test also shows automatic cut-off by the ESC when the voltage reached 7 V, indicating that the programmed full pack cut-off voltage never has to step in. The PCB hence only needs to act as an additional layer of safety and as a cut-off if one of the series connected cells falls below 2 V before the others.

It can be seen that the scaling of the voltage is not perfect, as there is a 4 V step from cell two to the full pack voltage, and that cell one only has approximately 2 V. This can likely be due to the large tolerances on the resistors used in the cell simulator. Ideally, the scaling factors in the ATMega328PB should be calibrated as batteries are connected.

4.3.2 Electrical dimensioning of structural battery pack

As stage 1 concludes, the impedance data from the chosen cell design, seen in Figure 4.2 is used to design the electrical system and estimate the required capacity of the structural battery pack. Using three series connected cell groups, each with nine parallel connected cells with $R_{ct} = 40\ \Omega$, $R_{\Omega} = 27\ \Omega$ and $C_{dl} = 20\ \mu F$, the IR drop was simulated, using an assumed target motor current of 140 mA. The simulated circuit with values calculated from equations 2.5-2.10 is seen with its resulting voltage response in Figure 4.14. The resulting capacity of the pack, is based on the GCD cycling approximately 58 mAh.

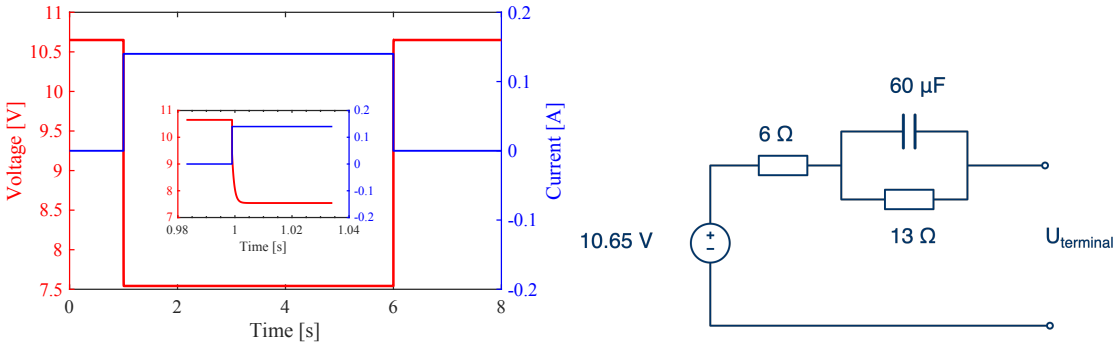

(a) **(b)**

Figure 4.14: (a) The resulting simulated IR drop from a 9p3s structural battery pack based on a Randles fit, (b) the simulated Randles circuit with calculated values.

This configuration assumes each cell is fully charged to 3.55 V. The IR drop is significant, but the voltage is kept at a level that is very suitable for the motor and ESC. However, the voltage will continue to rapidly decrease, as the high discharge current, equivalent to approximately 2C, will have a significant negative impact on the usable capacity in the batteries. Although the simulation gives no exact indication of the flight time, it can be seen that the terminal voltage seen by the ESC is sufficient to drive the motor at start-up. Hence, this cell configuration is used as a foundation when designing the fuselage and other surrounding systems.

4.3.3 Propeller performance evaluation

The measured thrust, speed, and current for the APC freeflight propeller bought off the shelf, the 3D printed DA4052 5x4.92(+5deg) propeller, and the carbon fibre in-house manufactured DA4052 5x4.92(+5deg) propeller along with the calculated thrust using the UIUC database values can be seen in Figure 4.15.

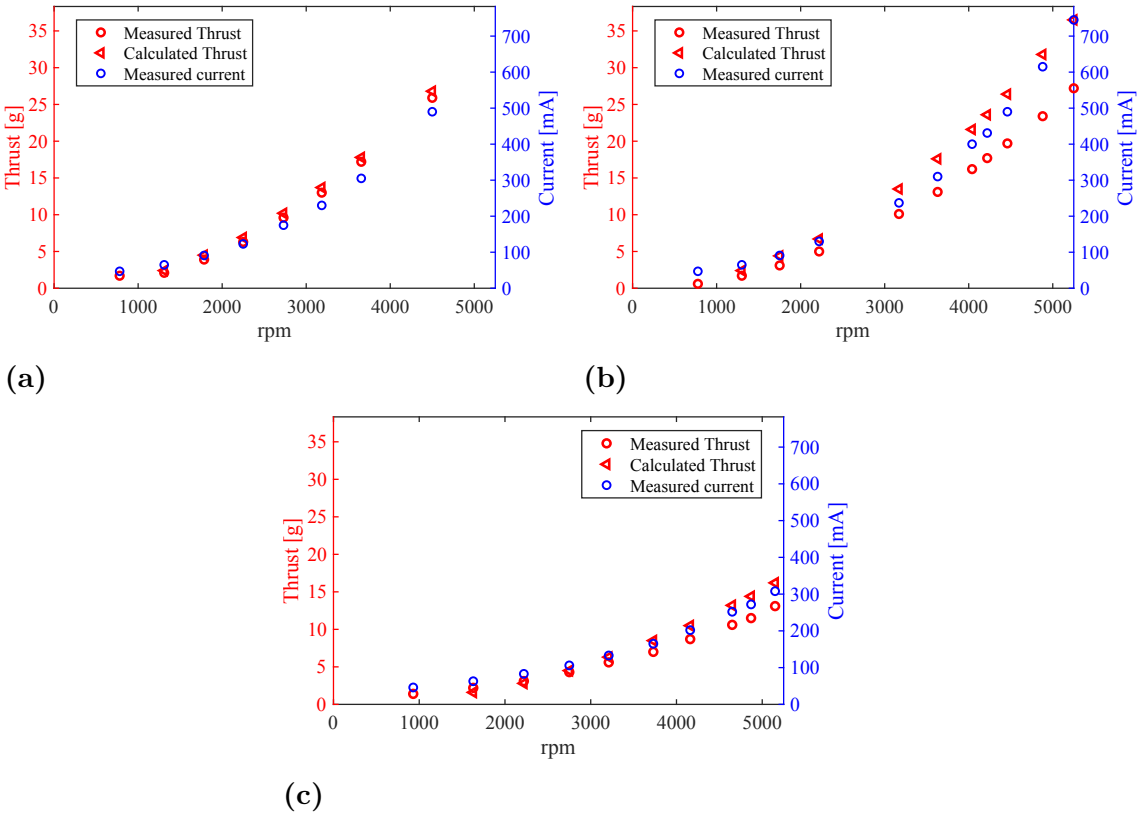

Figure 4.15: Performance of (a) composite DA4052 5x4.92(+5deg) propeller, (b) 3D-printed DA4052 5x4.92(+5deg) propeller, (c) APC Freeflight 4.2x4 propeller.

The difference in measured thrust and calculated thrust for the OTS propeller and composite propeller is in the range of margin of error, due to the limitations in the least count of the stroboscope, and due to inaccuracies in the test setup as discussed in Section 3.4. As expected, the 3D printed propeller performance diverges from the calculated performance due to the suboptimal geometrical accuracy the manufacturing method provides.

Interpolations of the current drawn by the motor under flight conditions for the CF propeller can be made by comparing the static power coefficient C_{P0} with the power coefficient C_P at the same rotational speed under forward flight. At 3800 rpm in static conditions, the current is approximately 340 mA as seen in Figure 4.15a and C_{P0} is 0.109. At a speed of 3800 rpm and forward velocity of 6 ms^{-1}, the C_P is 0.045. Assuming constant voltage and motor efficiency between these operating points, the current scales proportionally with C_P according to Equation 2.18, giving current drawn during cruise as 140.4 mA. This is a realistic number that can be used for making initial design calculations.

5
Conclusion and future work

This thesis has concentrated on developing a platform for a flying structural battery demonstrator, including all necessary subsystems, using the first generation of structural battery cells. The results demonstrate that this first generation, which employs a cellulose separator, is not suitable for use in an aircraft demonstrator because it lacks long-term electrochemical stability. Furthermore, the decision to restrict the project to commercially available electrodes as a time-saving strategy turned out to compromise not only the MFE but also the electrochemical reliability.

The finalised closed v-section aircraft structure prove the best for structural battery integration, due to the three sides offering flat surfaces for cell integration. The closed shape also provides the best mechanical properties, meaning that the aircraft can be kept light without the risk of mechanical failure.

While no major conclusion should be drawn from the cell results, due to the lack of robustness in the foundational cell topology, the stacked cells provide good power capabilities and energy density during the first stage of cell testing. This means that it could potentially be the best cell design for the aircraft demonstrator, although it must be re-evaluated if a new foundational cell topology is used, such as the all-fibre battery.

The electrical system gained a major advantage from using a commercial speed controller and motor, as the broad radio controlled hobby market offers a great deal of lightweight equipment. This meant a great amount of time could be saved. By designing a custom cell monitoring based on the minimum requirements for safe operation, and using only a pre-programmed speed sequence, the remaining electronics could be designed to minimzie complexity and weight, as indicated by the BOM. This played well with the demonstrator's performance requirements, as a low weight significantly reduces the current which has to be drawn from the cells.

Nevertheless, the final mechanical and electrical setup, which together constitute a complete flight platform, offers a strong foundation for future work using the latest generation of structural batteries. Drawing on the propeller benchmarking data, and assuming the power coefficient is reduced by half under dynamic conditions, the expected current consumption is estimated to be around 140 mA, for a conservatively assumed final aircraft mass of 100 g. This low current demand is a result of the successful lightweight design of all components, from the fuselage and propeller to the PCB.

Looking ahead, it would be highly valuable to test the cell formats presented here with the all-fibre structural battery, since the few double-layered cells that exhibit long-term electrochemical stability with the commercial LFP foil also display promising impedance characteristics and cell-level energy density. Now that cells can be produced using larger glass panels, exploring larger cell formats is also of great interest, as this would further reduce the mass fractions of the separator and current collector, thereby increasing cell-level energy density and lowering the overall system weight.

Additionally, future work could include estimating the expected flight time. The all-fibre battery is well-documented in terms of capacity retention at various C-rates. This information could be incorporated as an extra design parameter for the final structural battery pack to achieve the optimal trade-off between weight and flight time.

Another open challenge, that could not be tackled in this work due to the absence of sufficiently functional cells, is the development of a lightweight structural encapsulation of the cells to prevent moisture and oxygen ingress into the cells. Several strategies could be investigated, such as encapsulation via a glass fibre wet layup, or adding a cellulose or aluminium protective layer within an epoxy matrix around the cell, which can be directly cast in a silicone mould. These methods are still largely unstudied but represent promising avenues for future research.

Bibliography

[1] T. Kertscher, "Carry that weight? Electric vehicles outweigh gas cars but aren't main culprit of road wear," PolitiFact, Jun. 2023, accessed: 2026-04-07. [Online]. Available: https://www.politifact.com/article/2023/jun/21/carry-that-weight-electric-vehicles-outweigh-gas-c/

[2] L. E. Asp, K. Bouton, D. Carlstedt, S. Duan, R. Harnden, W. Johannisson, M. Johansen, M. K. G. Johansson, G. Lindbergh, F. Liu, K. Peuvot, L. M. Schneider, J. Xu, and D. Zenkert, "A structural battery and its multifunctional performance," *Advanced Energy and Sustainability Research*, vol. 2, no. 3, p. 2000093, 2021. [Online]. Available: https://advanced.onlinelibrary.wiley.com/doi/abs/10.1002/aesr.202000093

[3] R. Chaudhary, J. Xu, Z. Xia, and L. E. Asp, "Unveiling the multifunctional carbon fiber structural battery," 2024. [Online]. Available: https://doi.org/10.1002/adma.202409725

[4] K. Xu, "Nonaqueous liquid electrolytes for lithium-based rechargeable batteries," *Chemical reviews*, vol. 104, pp. 4303–417, 10 2004.

[5] J. U. Choi, N. Voronina, Y.-K. Sun, and S.-T. Myung, "Recent progress and perspective of advanced high-energy co-less ni-rich cathodes for li-ion batteries: Yesterday, today, and tomorrow," *Advanced Energy Materials*, vol. 10, no. 42, p. 2002027, 2020. [Online]. Available: https://advanced.onlinelibrary.wiley.com/doi/abs/10.1002/aenm.202002027

[6] H. Yu, X. Dong, Y. Pang, Y. Wang, and Y. Xia, "High power lithium-ion battery based on spinel cathode and hard carbon anode," *Electrochimica Acta*, vol. 228, pp. 251–258, 2017. [Online]. Available: https://www.sciencedirect.com/science/article/pii/S0013468617300968

[7] Y. Bi and D. Wang, "Revisiting olivine phosphate and blend cathodes in lithium ion batteries for electric vehicles," in *New Perspectives on Electric Vehicles*, M. Găiceanu, Ed. London: IntechOpen, 2021, ch. 8. [Online]. Available: https://doi.org/10.5772/intechopen.99931

[8] R. M. Jones, *Mechanics of Composite Materials*, 2nd ed. Washington, D.C.: Taylor & Francis, 1999.

[9] D. J. O'Brien, D. M. Baechle, and E. D. Wetzel, "Design and performance of multifunctional structural composite capacitors."

[10] M. S. Siraj, S. Tasneem, D. Carlstedt, S. Duan, M. Johansen, C. Larsson, J. Xu, F. Liu, F. Edgren, and L. E. Asp, "Advancing structural battery composites: Robust manufacturing for enhanced and consistent multifunctional performance," *Advanced Energy and Sustainability*

Research, vol. 4, no. 11, p. 2300109, 2023. [Online]. Available: https://advanced.onlinelibrary.wiley.com/doi/abs/10.1002/aesr.202300109

[11] J. Xu, Z. Geng, M. Johansen, D. Carlstedt, S. Duan, T. Thiringer, F. Liu, and L. E. Asp, "A multicell structural battery composite laminate," *EcoMat*, vol. 4, no. 3, p. e12180, 2022. [Online]. Available: https://onlinelibrary.wiley.com/doi/abs/10.1002/eom2.12180

[12] S. Nguyen, D. B. Anthony, T. Katafiasz, G. Qi, S. Razavi, E. Senokos, E. S. Greenhalgh, M. S. Shaffer, A. R. Kucernak, and P. Linde, "Manufacture and characterisation of a structural supercapacitor demonstrator," *Composites Science and Technology*, vol. 245, p. 110339, 2024. [Online]. Available: https://www.sciencedirect.com/science/article/pii/S0266353823004335

[13] L. Kong, R. Aalund, M. Alipour, S. I. Stoliarov, and M. Pecht, "Evaluating the manufacturing quality of lithium ion pouch batteries," *Journal of The Electrochemical Society*, vol. 169, p. 040541, 4 2022. [Online]. Available: https://iopscience.iop.org/article/10.1149/1945-7111/ac6539

[14] F. Schomburg, B. Heidrich, S. Wennemar, R. Drees, T. Roth, M. Kurrat, H. Heimes, A. Jossen, M. Winter, J. Y. Cheong, and F. Röder, "Lithium-ion battery cell formation: status and future directions towards a knowledge-based process design," *Energy Environ. Sci.*, vol. 17, pp. 2686–2733, 2024. [Online]. Available: http://dx.doi.org/10.1039/D3EE03559J

[15] P. Keil and A. Jossen, "Charging protocols for lithium-ion batteries and their impact on cycle life—an experimental study with different 18650 high-power cells," *Journal of Energy Storage*, vol. 6, pp. 125–141, 2016. [Online]. Available: https://www.sciencedirect.com/science/article/pii/S2352152X16300147

[16] D. Andre, M. Meiler, K. Steiner, C. Wimmer, T. Soczka-Guth, and D. Sauer, "Characterization of high-power lithium-ion batteries by electrochemical impedance spectroscopy. i. experimental investigation," *Journal of Power Sources*, vol. 196, no. 12, pp. 5334–5341, 2011, selected papers presented at the 12th Ulm ElectroChemical Talks (UECT):2015 Technologies on Batteries and Fuel Cells. [Online]. Available: https://www.sciencedirect.com/science/article/pii/S0378775311000681

[17] W. Choi, H.-C. Shin, J. M. Kim, J.-Y. Choi, and W.-S. Yoon, "Modeling and applications of electrochemical impedance spectroscopy (eis) for lithium-ion batteries," *J. Electrochem. Sci. Technol*, vol. 2020, pp. 1–13. [Online]. Available: https://doi.org/10.33961/jecst.2019.00528

[18] A. C. Lazanas and M. I. Prodromidis, "Electrochemical impedance spectroscopy, a tutorial," *ACS Measurement Science Au*, vol. 3, no. 3, pp. 162–193, 2023. [Online]. Available: https://doi.org/10.1021/acsmeasuresciau.2c00070

[19] M. Ozguc, E. Ipek, K. Aras, and K. Erhan, "Comprehensive analysis of pre-charge sequence in automotive battery systems," *Transactions on Environment and Electrical Engineering*, vol. 4, p. 1, 12 2019.

[20] W. Cao, S. Bukhari, and L. Aarniovuori, "Review of electrical motor drives for electric vehicle applications," *Mehran University Research Journal of Engineering and Technology*, vol. 38, pp. 525–540, 07 2019.

[21] "Introduction to brushless dc motor control: How three-phase inverters work - matlab & simulink." [Online]. Available: https://se.mathworks.com/campaigns/offers/next/introduction-to-brushless-dc-motor-control/how-three-phase-inverters-work.html

[22] "What is rc esc? what is bec/ubec? what does bec/ubec do? – rc models, diy hobby elektronics, arduino projects, rc airplanes." [Online]. Available: https://www.rcpano.net/2023/02/19/what-is-the-rc-esc-what-is-bec-ubec-what-does-bec-ubec-do/

[23] "Thobby m0802 kv27000 microwhoop motor indoor fpv drone." [Online]. Available: https://www.mepsking.shop/drone-parts/motors/thobby-m0802-kv27000-microwhoop-motor-indoor-fpv-drone.html

[24] N. Khan, C. A. Ooi, A. Alturki, M. Amir, Shreasth, and T. Alharbi, "A critical review of battery cell balancing techniques, optimal design, converter topologies, and performance evaluation for optimizing storage system in electric vehicles," *Energy Reports*, vol. 11, pp. 4999–5032, 2024. [Online]. Available: https://www.sciencedirect.com/science/article/pii/S2352484724002506

[25] J. D. J. Anderson, *Introduction to Flight*, 7th ed. New York: McGraw-Hill, 2011.

[26] J. G. Leishman. (2026) Introduction to aerospace flight vehicles. Licensed under CC BY-NC-ND 4.0. [Online]. Available: https://eaglepubs.erau.edu/introductiontoaerospaceflightvehicles/

[27] B. W. McCormick, *Aerodynamics, Aeronautics, and Flight Mechanics*, 2nd ed. New York: John Wiley & Sons, 1995.

[28] TeXtreme / Oxeon AB, "Woven carbon fabrics (0/90 and +/-45) product information," 2026, accessed: 2026-06-02. [Online]. Available: https://textreme.com/products/woven-fabrics/carbon

[29] Nils Malmgren AB, "Datablad nm infusion 693," Nils Malmgren AB, Technical Data Sheet, 2021. [Online]. Available: https://www.nilsmalmgren.se/wp-content/uploads/Datablad/TDS-S-NM-Infusion-693.pdf

[30] SHD Composite Materials Ltd, "Vtc401 epoxy component prepreg technical data sheet," SHD Composite Materials Ltd, Tech. Rep., 2023, accessed: 2026-06-01. [Online]. Available: https://shdcomposites.com/assets/prepregs/vtc401-tds-usa.pdf

[31] M. S. Selig, J. J. Guglielmo, A. P. Broeren, and P. Giguere, *Summary of Low-Speed Airfoil Data*. Virginia Beach, Virginia: SoarTech Publications, 1995, vol. 1.

[32] *Divinycell H Technical Data Sheet*, Diab Group, Sep. 2025. [Online]. Available: https://diab-media.azureedge.net/eyajkrhd/diab-divinycell-h-sep-2025-rev25-si.pdf

[33] "T-hobby am20 f3p airplane brushless motor." [Online]. Available: https://www.mepsking.shop/drone-parts/motors/am20-f3p-a-motor.html

[34] R. W. Deters, G. A. Krishnan, and M. S. Selig, "Uiuc propeller database, volume 2," https://m-selig.ae.illinois.edu/props/volume-2/propDB-volume-2.html, 2015, university of Illinois at Urbana-Champaign, accessed 2026-05-20.

[35] APC Propellers. (n.d.) 4.2x4. APC Propellers. [Online]. Available: https://www.apcprop.com/product/4-2x4/?v=f003c44deab6

[36] R. W. Deters, G. A. Krishnan, and M. S. Selig, "Reynolds number effects on the performance of small-scale propellers," in *32nd AIAA Applied Aerodynamics Conference*. American Institute of Aeronautics and Astronautics, 2014. [Online]. Available: https://m-selig.ae.illinois.edu/pubs/DetersAnandaSelig-2014-AIAA-2014-2151.pdf

[37] AddNorth. (2023) Pc blend ht lcf technical data sheet. [Online]. Available: https://storage.googleapis.com/addnorth-com.appspot.com/imgix/assets/production/TDS_pcblendhtlcf_utXzD2.pdf

[38] "Am series esc instruction manual." [Online]. Available: https://store.tmotor.com/images/file/20210926/1632645436360299.pdf?srsltid=AfmBOopmxo8CqHhYLhSJvE3SDw2Rfh3byUVFaoR2gBxP4EHsXksQ_nLe

[39] "Atmega328pb avr® microcontroller with core independent peripherals and picopower® technology," 2018.

[40] M. Sunna, "Bq76942 evaluation module," 2020. [Online]. Available: www.ti.com.

A

Off the shelf, donated, and electronic parts of the aircraft

(a)

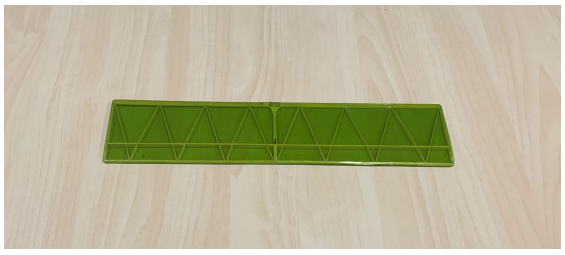

(b)

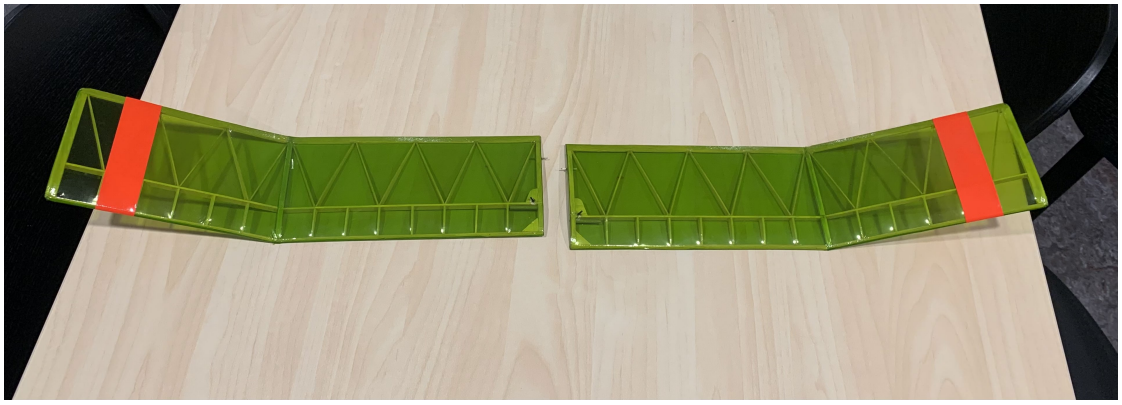

(c)

Figure A.1: (a) Vertical stabiliser, (b) horizontal stabiliser, and (c) wings donated by Erik Kullgren at Elitkomposit

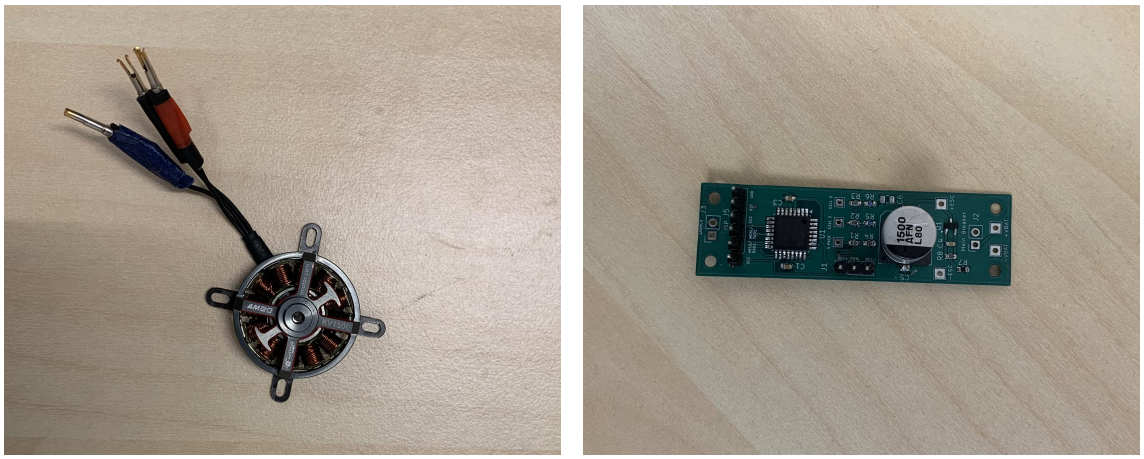

(a) **(b)**

Figure A.2: (a) OTS motor, (b) custom PCB

Table A.1: Bill of Materials (11) of all off-the-shelf, donated, and electronic components

Part Name	No. of Units	Mass per Unit (g)	Total Mass (g)
Wing	2	8.787	17.574
Horizontal stabiliser	1	5.123	5.123
Vertical stabiliser	1	1.504	1.504
Wing Spar	1	0.262	0.262
Motor + ESC	1	11.100	11.100
PCB	1	4.000	4.000
Rubber bands	3	0.464	1.392
Total			**40.955**

DEPARTMENT OF INDUSTRIAL AND MATERIAL SCIENCE
CHALMERS UNIVERSITY OF TECHNOLOGY
Gothenburg, Sweden
www.chalmers.se

CHALMERS
UNIVERSITY OF TECHNOLOGY